From *Operando* Raman Mechanochemistry to "NMR Crystallography": Understanding the Structures and Interconversion of Zn-Terephthalate Networks Using Selective ^{17}O-Labeling

César Leroy,* Thomas-Xavier Métro, Ivan Hung, Zhehong Gan, Christel Gervais, and Danielle Laurencin*

Read Online

ACCESS | Metrics & More | Article Recommendations | Supporting Information

ABSTRACT: The description of the formation, structure, and reactivity of coordination networks and metal−organic frameworks (MOFs) remains a real challenge in a number of cases. This is notably true for compounds composed of Zn^{2+} ions and terephthalate ligands (benzene-1,4-dicarboxylate, BDC) because of the difficulties in isolating them as pure phases and/or because of the presence of structural defects. Here, using mechanochemistry in combination with *operando* Raman spectroscopy, the observation of the formation of various zinc terephthalate compounds was rendered possible, allowing the distinction and isolation of three intermediates during the ball-milling synthesis of $Zn_3(OH)_4(BDC)$. An "NMR crystallography" approach was then used, combining solid-state NMR (^{1}H, ^{13}C, and ^{17}O) and density

functional theory (DFT) calculations to refine the poorly described crystallographic structures of these phases. Particularly noteworthy are the high-resolution ^{17}O NMR analyses, which were made possible in a highly efficient and cost-effective way, thanks to the selective ^{17}O-enrichment of either hydroxyl or terephthalate groups by ball-milling. This allowed the presence of defect sites to be identified for the first time in one of the phases, and the nature of the H-bonding network of the hydroxyls to be established in another. Lastly, the possibility of using deuterated precursors (*e.g.*, D_2O and d_4-BDC) during ball-milling is also introduced as a means for observing specific transformations during *operando* Raman spectroscopy studies, which would not have been possible with hydrogenated equivalents. Overall, the synthetic and spectroscopic approaches developed herein are expected to push forward the understanding of the structure and reactivity of other complex coordination networks and MOFs.
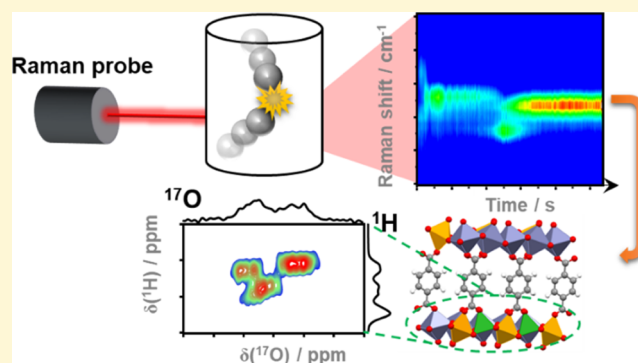
INTRODUCTION

In recent years, the use of mechanochemistry in material synthesis has undergone an exponential development. Ball-milling (BM) syntheses have notably proved to be of great interest in pharmaceutical materials screening, battery development, or even catalysis.[1,2] More than offering a drastic reduction of bulk-solvent use in the syntheses, it offers a precise control over the stoichiometry of the reaction, as well as simple and straightforward synthetic procedures.[3,4] However, because of the closed environment of mechanochemical reactions (especially when conducted in stainless steel jars), these syntheses are still considered as "black boxes". In this context, the last decade has seen the emergence of *in situ* time-resolved analysis techniques applied to BM syntheses, which allow the evolution of the reaction medium to be monitored without needing to interrupt the milling process and open the jar. Among them, two are of particular interest: powder X-ray diffraction (pXRD) and Raman spectroscopy.[5−11] While the first requires the use of a synchrotron beamline, the second can be set up in standard laboratories thanks to bench-top Raman

spectrometers and probes. Such systems permit reaction rates to be followed, complex reaction schemes to be understood, and can also shed light on the appearance of yet unknown/unobserved reaction intermediates.[12,13] Furthermore, these experimental installations can also be coupled with thermal imaging cameras to have an even more precise description of the course of the chemical reactions.[14,15] It is worth mentioning that meticulous kinetic studies from *operando* Raman spectroscopy experiments have been recently proposed.[16,17]

Metal−organic frameworks (MOFs) represent a major family of porous materials, with porosities that can exceed
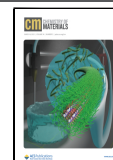
Table 1. Zn-BDC Compounds Studied in This Contribution, Together with Structural Details, as Initially Reported in the Corresponding Refs 41−44

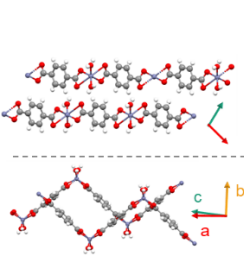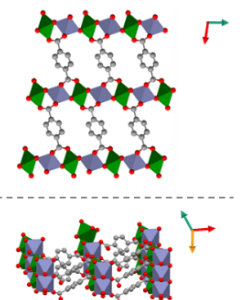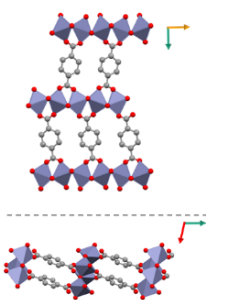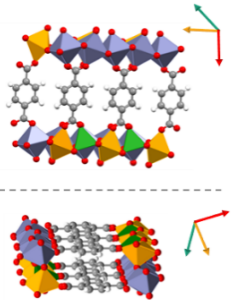| Designation	ZTA1	ZTA2a	ZTA2b	ZTA3
CCDC code(s)	DIKQET / 133475	ECATIO / 1520407 PUCYAO01	PUCYAO / 695449	PEKGAO / 295966
Reference	41	42	43	44
Reported formula	$Zn(BDC)(H_2O)_2$	$Zn_2(OH)_2(BDC)$	$Zn_2(OH)_2(BDC)$	$Zn_3(OH)_4(BDC)$
Space Group	$C2/c$	$C2/c$	$P2_1/c$	$C2/c$
Representation				
Metal centre geometry	Zn – Tetracoordinate	Zn1 – Hexacoordinate Zn2 – Hexacoordinate	Zn – Pentacoordinate	Zn1 – Tetracoordinate Zn2 – Pentacoordinate Zn3 – Hexacoordinate
BDC ligands & coordination	1 carboxylate environment Monodentate	1 carboxylate environment Bridging	1 carboxylate environment Bridging	2 carboxylate environments Bridging
Remarks	- Zig-zag Chain - 2 coordinated-H_2O - Coordination polymer	- Lamellar - 1 hydroxyl environment - No information on crystal preparation	- Lamellar - 1 hydroxyl environment - No hydrogen position reported	- Lamellar - 4 hydroxyl environments - No hydroxyl hydrogen position reported

50% of their volume. The impressive range of their applications extends from fuel/gas storage to catalysis or even cancer therapy.[18−20] Various synthetic routes have been developed for obtaining and/or shaping these materials, like solvothermal or microwave syntheses, and also mechanochemistry.[21−24] The numerous properties of MOFs being strongly and directly related to their crystallographic structures, it is then of primary importance to precisely control their synthesis to obtain pure phases through meticulous and reproducible procedures.[25] In this context, *in situ* monitoring experiments can help observe or even trap interesting intermediates. For example, recently, Jones et al. presented the use of *in situ* ¹H liquid-state NMR for observing the formation of a Ni-MOF.[26] Insights into the nucleation and crystal growth processes of this MOF were obtained through the kinetic studies carried out at different temperatures. Concerning MOFs formed by mechanosynthesis, a recent example by Karadeniz et al. revealed the interplay between MOF-525 and its polymorph PCN-223, two porphyrinic zirconium MOFs. In their case, *in situ* pXRD monitoring allowed the MOF-525 to be detected as an intermediate during the formation of PCN-223, depending on the synthetic conditions used.[27] A similar experimental

procedure also allowed the presence of metastable MOFs in the formation of *dia*-Zn(MeIm)₂ (MeIm: 2-methylimidazole) to be demonstrated.[6]

Among MOFs, those based on zinc (Zn-MOFs) have been the focus of much interest because of their high porosity and/ or interesting applications. In particular, because zinc is a biocompatible metal, zinc-containing materials such as the porous scaffold Zn-xWE43 (WE43 being a Mg alloy) or the $Zn_2(BDC)_2$(diazabicyclooctane) MOF (with BDC standing for 1,4-benzenedicarboxylate) have been studied as candidates for implants and drug delivery.[28,29] Furthermore, Zn-MOFs have shown great potential for applications as catalysts, anodes for lithium batteries, or materials for uranium adsorption/ detection.[30−32] Among the numerous Zn-MOFs described to date, coordination complexes based on Zn^{2+}-dicarboxylate motifs have been found to exist as a very broad diversity of structures.[33] For instance, the well-known structure of MOF-5 ($Zn_4O(BDC)_3$) exhibits 4-fold-coordinated zinc sites with bridging carboxylate functions, while MOF2 ($Zn_2(BDC)_2$) presents one 5-fold-coordinated zinc ion with four bridging oxygens from carboxylate ligands and one additional coordinated water molecule.[34,35] Interconversion between

these two structures has also been demonstrated in specific synthetic conditions (high pressure, temperatures up to 120 °C).[36] Furthermore, the different investigations performed so far on coordination networks involving Zn^{2+} ions and terephthalate ligands (noted Zn-BDC from hereon) have enabled many other structures to be described, *e.g.*, $Zn(BDC)(H_2O)$,[37] $Zn_3(OH)_4(BDC) \cdot 6H_2O$,[38] and $(Zn_3(BDC)_4 \cdot 4H_2O)_n$,[39] just to name a few. Here, we decided to focus our attention on four other Zn-BDC structures: a dihydrated zinc terephthalate coordination polymer, $Zn-(BDC)(H_2O)_2$,[40] and three lamellar phases involving terephthalate and hydroxyl ligands (see Table 1).

The $Zn(BDC)(H_2O)_2$ phase (noted here **ZTA1**) consists of a "zig-zag" arrangement of chains formed by distorted tetrahedral zinc environments, in which each Zn^{2+} ion is linked to two monodentate BDC ligands and two water molecules (Table 1). Regarding the three lamellar structures, two are polymorphs of general formula $Zn_2(OH)_2(BDC)$ (noted here as **ZTA2a** and **ZTA2b**). The structure of the latter polymorph (**ZTA2b**) has been more thoroughly described so far:[43] it exhibits only one penta-coordinated zinc environment, with well-ordered π-stacked BDC units. The structure of the other polymorph (**ZTA2a**), *a contrario*, reveals more uncertainties. In fact, although several articles have reported the presence of this phase (by looking at pXRD data), no consensus has been found in the literature about its structure. Rodríguez et al. attributed this compound to a distorted MOF-5 phase caused by a default in one of the binding modes of carboxylate groups to Zn^{2+}.[45] Thirumurugan and Rao observed this phase as an intermediate in their hydrothermal reactions when using a Zn/BDC 1/1 molar ratio but were not able to propose an exact formula for it.[46] Hirai et al. were unable to isolate a pure phase of this material but were able to detect it in a microwave synthesis when using a Zn/BDC ratio of 2/1 and working at specific pH (between 5.7 and 4.9).[38] In 2016, a crystal structure was reported in the Cambridge crystallography database (CCDC ECATIO), which matches the pXRD pattern of this same phase and corresponds to the $Zn_2(OH)_2(BDC)$ chemical formula (with a Zn/BDC ratio of 2/1). Unfortunately, no information on its synthesis could be found.[42] When looking at the crystallographic file, it appears that it corresponds to a lamellar structure with two distinct zinc sites in octahedral geometry, which are separated by one bridging oxygen belonging to a hydroxyl (Table 1). Between two layers, the BDC ligands exhibit a "zig-zag" configuration of the aromatic rings. Hence, both polymorphs differ by subtle modifications of the BDC arrangements, resulting in different coordination modes of the metal centers, and the **ZTA2a** phase displays a slightly smaller interlamellar spacing than **ZTA2b** (about 10.1 *vs* 10.8 Å, respectively) (see Table 1). Lastly, the fourth phase of interest in this work is $Zn_3(OH)_4(BDC)$ (noted **ZTA3**).[44] This other lamellar Zn-hydroxide terephthalate is formed in a 3/1 Zn/BDC stoichiometry. Three distinct zinc environments were found to be present in the Zn–O polyhedra layers (with tetra/penta/hexacoordination, according to the initially reported crystallographic file), which are connected to each other through terephthalate and hydroxyl anions.

Diffraction techniques remain, at the moment, the most common analytical tool to obtain structural information on Zn-BDC MOFs. However, preparing good-quality crystals can be very challenging. Moreover, providing exact positions for hydrogen atoms from pXRD data remains an issue, and only two out of the four reported structures in Table 1 fully report hydrogen positions (aromatics and hydroxyls/water). In complement to XRD, chemical and structural information on these phases can also be obtained through FTIR spectroscopy. For example, the O–H stretching modes of hydroxyls and water molecules are easily observed above 3000 cm^{-1} and can inform on the H-bond networks in presence. Moreover, the C–O stretching modes of the carboxylate groups are identified by the presence of antisymmetric and symmetric vibrations (noted $\nu_{as}(COO^-)$ and $\nu_s(COO^-)$) between 1650–1540 and 1450–1360 cm^{-1}, respectively, and information on the binding mode of the carboxylate ligands to zinc metal centers can *a priori* be proposed on the basis of the difference in wavenumbers between these two frequencies ($\Delta = \nu_{as}(COO^-) - \nu_s(COO^-)$).[47,48] However, very few articles have used solid-state NMR (ssNMR) techniques to probe the local environment of the atoms in Zn-BDC structures, even for some of the more readily observable isotopes such as ^1H and ^{13}C.[37,49−51] This can be seen as surprising considering that the use of ssNMR alongside XRD analyses is more and more frequent to elucidate the structure of MOFs and coordination polymers, including phases prepared using mechanochemistry,[52−54] such as MOF crystal-glass composites (MIL-53/ZIF-62),[55] cadmium-imidazole ZIFs,[54] or even paramagnetic MOFs (*e.g.* Ni(II)-MOF-74, bimetallic ZnCu-MOF-74).[56,57] More generally speaking, such techniques could help numerous debates, some of which will be discussed more extensively later in this contribution, which still remain about such zinc structures and their intermediates.

To further elucidate the details of the structure of these phases, ^{17}O ssNMR is a very attractive tool. Oxygen-17 is a spin-5/2 quadrupolar nucleus of low natural abundance (0.04%), which presents a very wide chemical shift range (exceeding 1000 ppm) and also a very wide variation of quadrupolar interaction (QI) parameters (C_Q, η_Q). Moreover, recent investigations have shown that ^{17}O ssNMR spectroscopy can be of high interest for studying the structure of coordination polymers and MOFs.[58−61] For example, Martins et al. have shown the powerful use of ultra-high-field ^{17}O ssNMR experiments (35.2 T) applied on ^{17}O-enriched Mg and Al MOFs (α-$Mg_3(HCOO)_6$ and MIL-53(Al)). Impressively, they were able to distinguish up to 12 inequivalent oxygen sites for as-made and activated phases of α-$Mg_3(HCOO)_6$.[62] While ^{17}O ssNMR is still not routinely used to investigate the structure of MOFs, our recent developments of cost-efficient ^{17}O-labeling schemes using mechanochemistry,[60,63,64] including for carboxylic ligands like terephthalic acid,[65] imply that such nonroutine NMR now become conceivable for studying Zn-BDC structures like those in Table 1.

In this contribution, we report a detailed investigation of the structure and interconversion between the four aforementioned Zn-BDC systems (**ZTA1**, **ZTA2a**, **ZTA2b**, and **ZTA3**) synthesized using mechanochemistry. We first show how by modifying the initial stoichiometry of the reaction, and carefully monitoring the course of the BM reactions using *operando* Raman spectroscopy and thermal analysis of the milling jar, each of these different phases can be easily isolated in a pure form and subsequently studied by *ex situ* methods (FTIR, powder X-ray diffraction, multinuclear ssNMR), allowing further information about their structures to be gained. Moreover, we then demonstrate for the first time how, by using this synthetic methodology, it becomes possible to perform selective ^{17}O isotopic labeling of the different types of

Table 2. Synthetic Details for BM Experiments of Zn-BDC Compounds[a]

code name	formula	m_{ZnO} (mg)	m_{H_2BDC} (mg)	V_{H_2O} (μL)	milling parameters	
					frequency (Hz)	duration (min)
ZTA1	Zn(BDC)(H$_2$O)$_2$	129.9	265.1	115	30	30
		1.59 mmol	1.59 mmol	6.38 mmol		
		1 equiv	1 equiv	4 equiv		
ZTA2a	Zn$_2$(OH)$_2$(BDC)	178.4	182.1	40	50	20
		2.19 mmol	1.09 mmol	2.22 mmol		
		2 equiv	1 equiv	2 equiv		
ZTA2b	Zn$_2$(OH)$_2$(BDC)	197.8	201.9	350	50	90
		2.43 mmol	1.21 mmol	19.43 mmol		
		2 equiv	1 equiv	16 equiv		
ZTA3	Zn$_3$(OH)$_4$(BDC)	262.1	178.4	310	50	90
		3.22 mmol	1.07 mmol	17.21 mmol		
		3 equiv	1 equiv	16 equiv		
			^{17}O-Labeled Compounds			
ZTA1-*BDC	Zn(BDC)(H$_2$O)$_2$	34.0	71.0*	17	50	5
		0.42 mmol	0.42 mmol	0.94 mmol		
		1 equiv	1 equiv	2 equiv		
ZTA2a-*BDC	Zn$_2$(OH)$_2$(BDC)	60.9	63.6*	15	50	12
		0.75 mmol	0.37 mmol	0.83 mmol		
		2 equiv	1 equiv	2 equiv		
ZTA2a-*OH		178.4	182.1	40*	50	20
		2.19 mmol	1.10 mmol	2.20 mmol		
		2 equiv	1 equiv	2 equiv		
ZTA2b-*OH	Zn$_2$(OH)$_2$(BDC)	171.2	174.7	40*	50	90
		2.10 mmol	1.05 mmol	2.20 mmol		
		2 equiv	1 equiv	2 equiv		
ZTA3-*BDC	Zn$_3$(OH)$_4$(BDC)	121.1	84.3*	50	50	90
		1.49 mmol	0.49 mmol	2.77 mmol		
		3 equiv	1 equiv	5 equiv		
ZTA3-*OH		119.6	81.4	50*		
		1.47 mmol	0.48 mmol	2.77 mmol		
		3 equiv	1 equiv	5 equiv		
			Deuterated Compounds			
ZTA1-d_4BDC	Zn(d_4BDC)(H$_2$O)$_2$	125.0	262.0^d	315	30	15
		1.54 mmol	1.54 mmol	17.48 mmol		
		1 equiv	1 equiv	11.2 equiv		
ZTA2a-d_4BDC	Zn$_2$(OH)$_2$(d_4BDC)	197.4	207.5^d	350	50	90
		2.42 mmol	1.22 mmol	19.43 mmol		
		2 equiv	1 equiv	16 equiv		
ZTA2b-OD	Zn$_2$(OD)$_2$(BDC)	188.1	192.8	335^d	50	90
		2.31 mmol	1.16 mmol	18.47 mmol		
		2 equiv	1 equiv	16 equiv		
ZTA3-d_4BDC	Zn$_3$(OH)$_4$(d_4BDC)	242.0	168.7^d	90	50	90
		2.97 mmol	0.99 mmol	5.00 mmol		
		3 equiv	1 equiv	5 equiv		
ZTA3-OD	Zn$_3$(OD)$_4$(BDC)	250.7	171.1	350^d		
		3.08 mmol	1.03 mmol	19.06 mmol		
		3 equiv	1 equiv	19 equiv		

[a]"*" is used for ^{17}O-labeled materials and "d" is used for deuterated materials (prepared from D$_2$O or d_4-BDC precursors).

oxygen environments in such MOF structures (by enriching either the water/hydroxyl ligands or the carboxylate ones), thereby opening the way to a level of structural insight, which had not been achieved before. Lastly, we show how the combination of high-resolution ^{17}O NMR analysis of these compounds and *ab initio* calculations of NMR parameters using the gauge-including projector-augmented wave method (GIPAW) can improve and/or correct the structural models of these phases, thereby paving the way to other investigations on

the structure/property relationships in complex coordination networks and MOFs.

■ MATERIALS AND METHODS

Reagents. The following commercial precursors were used as received without further purification: terephthalic acid (C$_8$H$_6$O$_4$, Janssen Chemicals, 98% purity, noted here H$_2$BDC), deuterated terephthalic acid (C$_8$D$_4$H$_2$O$_4$, with deuteration on the aromatic H positions only, Cambridge Isotope Laboratories, 98% purity, noted here d_4-BDC), ZnO (particle size < 5 μm, Sigma-Aldrich, 99.9%

purity), and D$_2$O (Sigma-Aldrich, 99.9% purity).^{17}O-labeled water (with ∼40, 70, or ∼90% ^{17}O-enrichment) was purchased from CortecNet.

^{17}O-enriched H$_2$BDC was prepared using two different mixer mills: either a vibratory mixer mill (Restch MM400 apparatus, as published elsewhere)[65] or by scaling-up the procedure using a planetary ball mill (Fritsch P7 apparatus), as described below.

H$_2$BDC-Enrichment in a Planetary Mixer Mill (Fritsch P7). H$_2$BDC (330 mg, 1.98 mmol, 1.0 equiv) and CDI (708.6 mg, 4.37 mmol, 2.2 equiv) were introduced into the stainless steel grinding jar (20 mL inner volume), to which 80 stainless steel beads (5 mm diameter) were then added. The jar was closed and subjected to grinding for two cycles of 10 min at 500 rpm, with a break of 30 min between each cycle in the P7 planetary ball mill. ^{17}O-labeled (91.5%, 106 μL, 5.96 mmol, 3.0 equiv) water was then added into the jar, and the mixture was subjected to further grinding for two cycles of 10 min at 500 rpm, with a break of 30 min between each cycle. To help recover the product, nonlabeled water (2 mL) was added into the jar, and the content was subjected to grinding for 1 min at 500 rpm. Then, the suspension was transferred to a beaker (together with 9 mL of nonlabeled water used here to rinse the jar). The medium was acidified under stirring to pH ∼ 1 with an aqueous solution of HCl (6 M, 44 drops). The white precipitate was immediately filtered on a glass frit, washed (3 × 2 mL of 1 M HCl and then 3 × 2 mL of ultrapure water), and then dried under vacuum. Yield: 312.7 mg (∼95%). Enrichment yield: 84%, enrichment level: 38.7%, as determined by the MS.

Mechanochemical Syntheses of Zn-BDC Networks. The Fritsch Pulverisette-23 (P23) vertical mixer mill was used in all reactions. BM syntheses were conducted in 10 mL inner-volume Perspex jars,[7] with two 10 mm diameter zirconia beads.

A typical mechanochemical synthesis was performed as follows. First, ZnO was introduced into a Perspex jar followed by H$_2$BDC (see Table 2 for exact masses). Both powders were gently mixed with a spatula before adding the two zirconia beads. Then, the appropriate amount of water was added. The jar was quickly closed, and parafilm was added to cover the junction of top/bottom parts of the jar to avoid any leaks as well as to increase air/water tightness. The system was then subjected to grinding for milling times ranging from 5 to 90 min in the P23 mixer mill operating at 30 or 50 Hz. The reactor was then opened, and the resulting compound was left to dry in air for several hours. The solid powder was subsequently recovered by scraping the edges of the reactor and beads with a spatula. All samples were obtained as white powders. After several uses, reactors can exhibit signs of erosion; however, no trace of Perspex was detected in the final compounds by ^{13}C ssNMR and *ex situ* Raman spectroscopy.

Further details on the amounts of reagents and milling conditions used to isolate each of the four phases, in their nonlabeled, ^{17}O-labeled, or deuterated forms, are provided in Table 2. It is worth noting that for the synthesis of ^{17}O-labeled compounds, amounts of reagents were reduced to further decrease the cost of obtaining an enriched material for ssNMR analyses.

"Routine" Characterizations of the Different Phases. Powder XRD analyses were performed on an X'Pert MPD diffractometer using Cu Kα_1 radiation (λ = 1.5406 Å), with the operation voltage and current maintained at 40 kV and 25 mA, respectively. Diffractograms were recorded between 2θ = 5 and 50° in the Bragg–Brentano configuration, with a step size of 0.050° and a time per step of 60 s.

Infrared (IR) spectra were recorded on a Perkin Elmer Spectrum 2 FTIR spectrometer, using the ATR measurement mode (4000–400 cm^{-1} range, four repetitions).

Operando **Raman Spectroscopy and Thermal Analysis.** In this manuscript, we use the term *operando* to insist on the fact that spectroscopic measurements were acquired during the milling (and without stopping the milling), as opposed to *in situ* analyses, which can be performed on a medium when the milling is stopped for a few seconds/minutes.[66]

The Raman measurements were performed with a WP 785 ER Raman spectrometer (Wasatch Photonics) using an IPS (Innovative

Photonic Solutions) laser source (working at ∼300 mW, wavelength of λ = 785 nm) and a contactless probe head (the probe's focal length is 11 mm for a 1 mm diameter spot). The positioning of the Raman probe was optimized such that the focus of the laser was localized at the inner jar wall. A laser exposure time of 5 s with five accumulations was chosen, and spectrum collection was repeated every 30 s during the milling time. Raman spectra were collected across a range from 220 to 3120 cm^{-1}, and a dark spectrum (laser OFF) was also recorded before starting the experiment and directly subtracted from the recorded spectra. No degradation of the jar and/or the compound by the laser was observed during the *operando* Raman experiments. The thermal imaging camera showed that during the milling, the laser beam did not prompt any additional heat around its focal point on the Perspex jar walls (compared to the jar's overall temperature). Moreover, no noticeable degradation of the reagents and products was observed under the operating conditions used here for *operando* Raman analyses. The obtained Raman spectra were processed with the OriginPro 2021 program. Baseline correction (asymmetric least-squares smoothing) was first applied to each spectrum, and then normalization of the signal of the Perspex jar (at 1728 cm^{-1} where no overlapping from reagents nor product is expected) was performed, prior to the subtraction of the signal of the vibrating empty jar (see Supporting Information Figure S1). The reproducibility of the kinetic measurements performed is illustrated in Figure S2.

Temperature measurements were carried out using an OPTRIS PI450i thermal imaging camera. The optical resolution of the device is 382 × 380 pixels. The temperature accuracy measured using this system is estimated to be about ±2 °C. Four different temperatures were recorded every 2 s during the milling, focusing on three to four different areas, corresponding to the top, center, and bottom of the jar, and also to the "hot spot" at each time point.

Cautionary remarks: the laser source used here is designed as a class IV during all procedures of operation, maintenance, and service, meaning that safety measures must be taken accordingly. The use of laser-specific safety goggles is required when operating this laser, as failure to wear appropriate eye protection may result in permanent eye damage. Caution must be taken to never look directly into the laser beam and make sure the laser direction points toward the wall. The power range for the laser is 0−580 mW. Measurements presented in this contribution were performed at ∼300 mW in a dedicated isolated dark room with proper safety signs on the door, and operators received specific security training before using this equipment.

Solid-State NMR. *^{1}H ssNMR.* ^{1}H ssNMR experiments were performed on a Varian VNMRS 600 MHz (14.1 T) NMR spectrometer, using a Varian 3.2 mm probe tuned to ^{1}H (599.82 MHz). Spectra were recorded under magic angle spinning (MAS) conditions, with a spinning speed of 16 kHz and under a regulated airflow (0 °C). A ^{1}H direct excitation pulse of 3.3 μs was used. Recycle delays used for the Zn-BDC compounds were 4 and 15 s for pure H$_2$BDC. Additional ^{1}H MAS NMR experiments were performed on a Bruker Avance NEO 850 MHz (20.0 T) NMR spectrometer, using a Bruker 1.3 mm probe, tuned to ^{1}H (850.23 MHz), with a spinning speed of 60 kHz. Adamantane was used as a secondary reference for setting ^{1}H chemical shifts (δ_{iso} = 1.8 ppm with respect to tetramethylsilane).

^{13}C ssNMR. ^{13}C ssNMR experiments were performed on a VNMRS 600 MHz (14.1 T) NMR spectrometer, using a Varian 3.2 mm HX probe tuned to ^{1}H (599.82 MHz) and ^{13}C (150.81 MHz). All one-dimensional (1D) ^{13}C NMR spectra consist of cross-polarization experiments (CP) under MAS conditions, with spinning frequencies from 4 to 15 kHz. A ^{1}H excitation pulse of 3.3 μs was used prior to a ramped spin-lock pulse of 5 ms contact time. Acquisition was performed under spinal-64 ^{1}H-decoupling (∼75 kHz RF). Recycle delays used for the Zn-BDC compounds were 4 and 15 s for pure H$_2$BDC. ^{13}C chemical shifts were referenced to adamantane used as a secondary reference (high-frequency peak at 38.5 ppm with respect to tetramethylsilane).

^{17}O ssNMR. ^{17}O ssNMR experiments were first performed on all samples on a Varian VNMRS 600 MHz (14.1 T) NMR spectrometer, using either Varian 3.2 mm HX or HXY probes, or a Phoenix 3.2 mm

Table 3. Main Acquisition Parameters for ^{17}O NMR Experiments

sample	field (T)	$\varnothing_{rotor}$ (mm)	expt	ν_{rot} (kHz)	D1 (s)	NS (/#t1)	ν_{RF} (kHz)	pulses (μs)	dec {^1H} (kHz)
ZTA1-*BDC	14.1	3.2	DFS-One pulse	18	2	1024	~40	2	75
	20.0	3.2	DFS-One pulse	14.286	4	256	10	8.33	60
ZTA2a-*BDC	9.4	3.2	DFS-One pulse	18	1	20480	~40	2	50
	14.1	3.2	DFS-One pulse	18	1	6144	~40	2	75
	18.8	3.2	MQMAS	16	5	768/22	~16	3/1/5	62.5
	20.0	4	DFS-One pulse	14.286	1	4096	10	8.33	60
ZTA2a-*OH	9.4	3.2	DFS-One pulse	18	2	512	~40	2	50
	14.1	3.2	DFS-One pulse	18	2	3072	~40	2	75
	20.0	4	DFS-One pulse	14.286	2	256	10	8.33	60
ZTA2b-*OH	9.4	3.2	DFS-One pulse	18	4	3072	~40	2	50
	14.1	3.2	DFS-One pulse	18	4	1024	~40	2	75
	20.0	4	DFS-One pulse	14.286	4	512	10	8.33	60
ZTA3-*BDC	9.4	3.2	DFS-One pulse	18	2	6144	~40	2	50
	14.1	3.2	DFS-One pulse	18	2	12288	~40	2	75
	18.8	3.2	MQMAS	16	5	768/32	~16	3/1/5	62.5
	20.0	4	DFS-One pulse	14.286	2	1024	10	8.33	60
		1.3	(DFS) D-HMQC	60	4	9216/24	20	4.167/8.33	75
ZTA3-*OH	9.4	3.2	DFS-One pulse	18	4	10240	~40	2	50
	14.1	3.2	DFS-One pulse	18	4	1024	~40	2	75
	18.8	3.2	MQMAS	16	5	480/32	~16	3/1/5	62.5
	20.0	4	DFS-One pulse	14.286	4	256	10	8.33	60
		1.3	(DFS) D-HMQC	60	2	1536/23	20	4.167/8.33	75

probe, tuned to ^1H (599.82 MHz) and ^{17}O (81.31 MHz). Spectra were recorded under MAS conditions under a regulated airflow (0 °C), with spinning speeds ranging from 16 to 20 kHz, depending on the sample. Additional ^{17}O MAS NMR experiments were performed at lower field on a VNMRS 400 MHz (9.4 T) NMR spectrometer, using a Varian 3.2 mm HXY probe tuned to ^1H (399.92 MHz) and ^{17}O (54.21 MHz). Moreover, higher-field ^{17}O NMR analyses were performed first on a Bruker Avance NEO 850 MHz (20.0 T) NMR spectrometer, using Bruker 1.3 or 4 mm probes tuned to ^1H (850.23 MHz) and ^{17}O (115.26 MHz) or on a Bruker Avance III HD 800 MHz (18.8 T) NMR spectrometer using a 3.2 mm Low-E probe spinning at 16 kHz ($\nu_L(^1H)$ = 800.12 MHz and $\nu_L(^{17}O)$ = 108.47 MHz) to perform multimagnetic field data fitting (see Supporting Information Figures S14−S17). A double frequency sweep (DFS) excitation scheme was used consisting of a 1 ms pulse with a sweep between 1 MHz and 50 kHz[67−69] for ^{17}O-signal enhancement (when possible) prior to the excitation pulse, and spinal-64 ^1H-decoupling was applied during acquisition. The acquisition parameters used for each sample (including number of scans and recycle delay D1) can be found in Table 3. The D-HMQC (dipolar-heteronuclear multiple-quantum coherence) sequence used an $SR4_1^2$ recoupling scheme on the ^1H channel with a radio-frequency field of twice the spinning speed; the detection is performed on the ^{17}O channel.[70] ^{17}O chemical shifts were referenced externally to D_2O at −2.7 ppm (or tap water at 0.0 ppm).

The NMR parameters were obtained by fitting the spectra using DMfit.[71]

NMR Conventions. In this article, the "Herzfeld−Berger" convention is used to describe the magnitude of the chemical shift anisotropy (CSA) arising from the magnetic shielding interaction.[72] The isotropic chemical shift (δ_{iso}), span (Ω), and skew (κ) are given as follows

$$\delta_{iso} = \frac{(\delta_{11} + \delta_{22} + \delta_{33})}{3} \tag{1}$$

$$\Omega \approx \delta_{11} - \delta_{33} \ (\Omega \geq 0) \tag{2}$$

$$\kappa = \frac{3(\delta_{22} - \delta_{iso})}{\Omega} \ (-1 \leq \kappa \leq +1) \tag{3}$$

The principal components of the chemical shift tensor are ordered as follows: $\delta_{11} \geq \delta_{22} \geq \delta_{33}$.

The quadrupolar interaction is described by two parameters, the quadrupolar coupling constant (C_Q) and the asymmetry parameter (η_Q)

$$C_Q = \frac{eQV_{33}}{h} \tag{4}$$

$$\eta_Q = \frac{V_{11} - V_{22}}{V_{33}} \tag{5}$$

Here, V_{11}, V_{22}, and V_{33} are the principal components of the traceless electric field gradient (EFG) tensor, with $|V_{33}| \geq |V_{22}| \geq |V_{11}|$, e is the fundamental electronic charge, Q is the nuclear quadrupole moment, and h is Planck's constant.

GIPAW-DFT Calculations. The unit cell parameters were set to the X-ray diffraction parameters and kept fixed during geometry optimizations to ensure consistency between experimental and optimized structures. Missing protons (in CCDC PUCYAO and PEKGAO structures) were initially positioned to be consistent with the expected structure of the system, and successively, only protons and then all atomic positions were relaxed with the VASP (Vienna ab initio simulation package) code[73] based on the Kohn−Sham density functional theory (DFT) and using a plane-wave pseudopotential approach. For the two structures mentioned above, several initial OH proton positions were tested. The NMR parameters were then calculated within the Kohn−Sham DFT using the QUANTUM-ESPRESSO code,[74,75] keeping the atomic positions equal to the values previously calculated with VASP. The PBE generalized gradient approximation[76] was used, and the valence electrons were described by norm-conserving pseudopotentials[77] in the Kleinman−Bylander form.[78] The shielding tensor was computed using the gauge-including projector-augmented wave (GIPAW) approach,[79] which enables the reproduction of the results of a fully converged all-electron calculation.[80] The isotropic chemical shift δ_{iso} is defined as $\delta_{iso} = -[\sigma - \sigma^{ref}]$, where σ is the isotropic shielding and σ^{ref} is the isotropic shielding of the same nucleus in a reference system. For ^1H, ^{13}C, and ^{17}O, previously used referencing was adopted using glycine,[81] calcite,[82] and a series of silicates,[63] respectively. Diagonalization of the symmetrical part of the calculated tensor then provides its principal components σ_{11}, σ_{22}, and σ_{33} from which the chemical shift
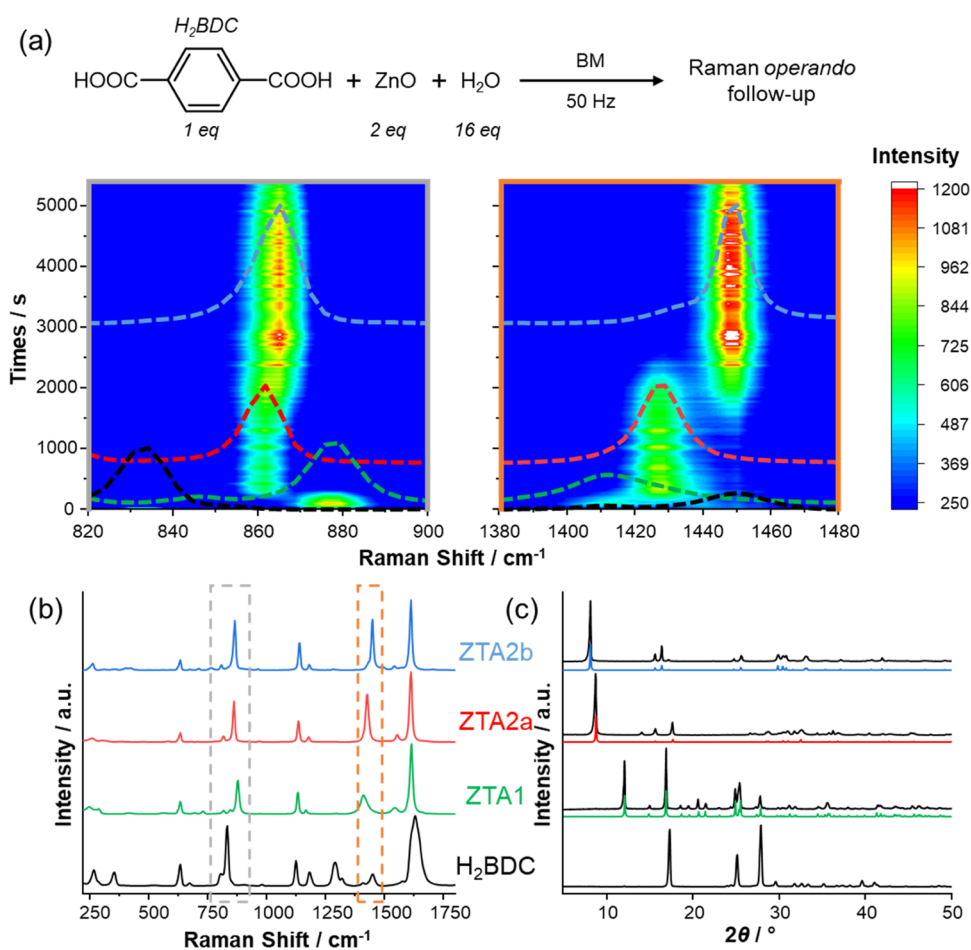
Figure 1. (a) Top: starting compounds used for the *operando* experiment with their respective equivalents and milling conditions. Bottom: time-resolved *operando* Raman spectra of two selected areas (gray and orange, see panel (b)): 820–900 cm^{-1} range on the left and 1380–1480 cm^{-1} range on the right (see Figure S2 for repetitions of the analysis in this zone); two-dimensional (2D) plots have been overlapped with spectra from panel (b). (b) Experimental *ex situ* Raman spectra of **H$_2$BDC** (in black), **ZTA1** (in green), **ZTA2a** (in red), and **ZTA2b** (in blue) when isolated under the milling conditions reported in Table 2. (c) Experimental *ex situ* pXRD diffractograms of the corresponding "pure" compounds when isolated under the milling conditions reported in Table 2 (in black), and comparisons with the simulated pXRD data for these Zn-BDC phases (colored lines; pXRD simulated from available CIF files in the CCDC database, as reported in Table 1).

components δ_{11}, δ_{22}, and δ_{33} can be calculated. The principal components V_{xx}, V_{yy}, and V_{zz} of the electric field gradient (EFG) tensor are obtained by diagonalization of the tensor. The quadrupolar interaction can then be characterized by the quadrupolar coupling constant C_Q and the asymmetry parameter η_Q, which are defined previously. The experimental value of the quadrupole moment of ^{17}O ($Q = -25 \times 10^{-30}$ m^2) was used to calculate C_Q.[83]

■ RESULTS AND DISCUSSION

Given the rich variety of structures involving Zn^{2+} and BDC ligands, in terms of Zn/BDC ratios, H$_2$O or OH species linked to the Zn^{2+}, and also carboxylate coordination modes, we decided to investigate the formation of these compounds using mechanochemistry, a synthetic method that had not yet been tested in a systematic way for these phases. The general idea was to see if conditions allowing each of these phases to be isolated in a pure form and high yield could be achieved using mechanochemistry. Coupled with the use of ^{17}O-enriched precursors, this approach would allow all of the different forms of Zn-BDC phases to be analyzed with an unprecedented level of detail, thereby providing novel information in the debate related to the structures of these materials.

Formation and Isolation of Zinc (Hydroxyl-) Terephthalate Coordination Complexes. *Observation of Several Intermediate Phases Using Operando Raman Analyses.* The three reagents, namely, H$_2$BDC, ZnO, and H$_2$O, were introduced in a Perspex milling jar to enable the monitoring of different vibration bands by Raman spectroscopy. An illustrative example of the formation of various Zn-BDC phases in a one-pot mechanochemistry synthesis is shown in Figure 1 for a ZnO/H$_2$BDC/H$_2$O stoichiometry of 2/1/16. In Figure 1a, the evolution of the Raman signals during the milling for two selected regions of the spectra is presented after data processing (see the Materials and Methods Section for more information). It is worth noting that water plays multiple roles in this system: (i) it is directly involved in the reaction, as a reagent, by forming complexes with the Zn^{2+} cations and in some cases leads to the formation of coordinated hydroxyls, (ii) it plays the role of a liquid-assisted grinding (LAG) agent, allowing a better mixing of the solid reagents and thus a better efficiency of the milling process,[84,85] (iii) it guarantees the formation of paste-like materials during the milling, which will be homogeneously spread over the inner surfaces of the milling jar. The latter point is of great importance for the *operando*
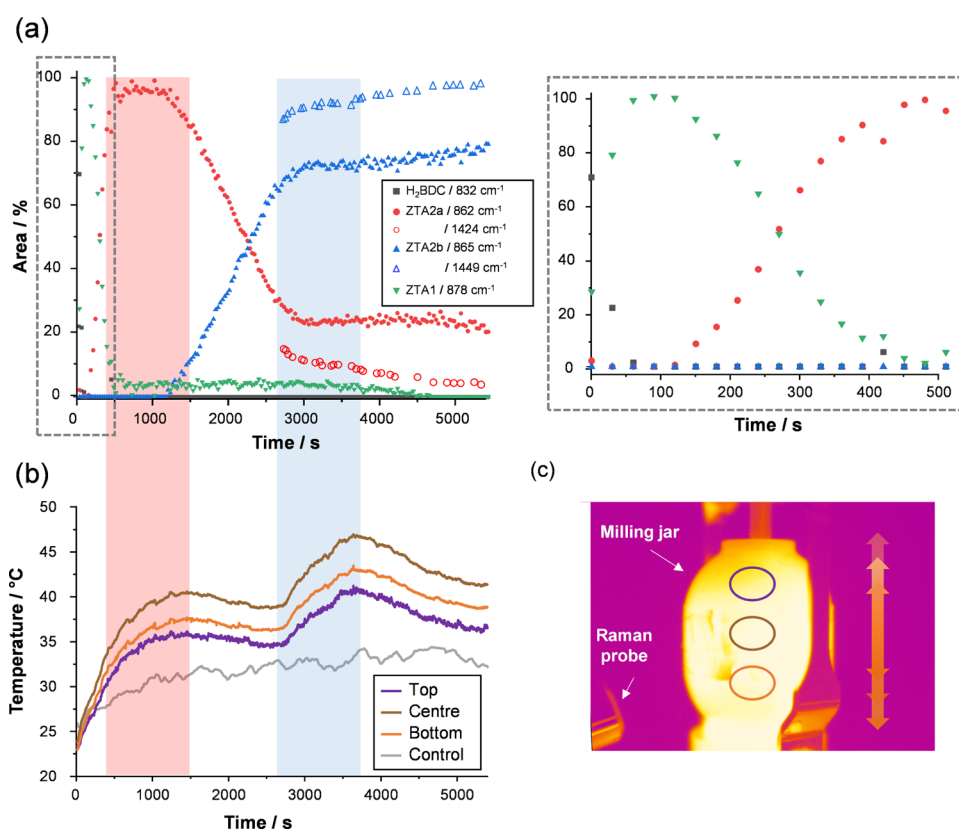
Figure 2. (a) Reaction profiles corresponding to signals highlighted in Figure 1b. Empty symbols (**ZTA2a** and **ZTA2b** at 1424 and 1449 cm^{-1}, respectively) are shown only for the last half of the milling time for clarity. The inset on the right-hand side corresponds to a zoom of the first 500 s of the time-resolved Raman experiment. (b) Temperature profiles of three different areas of the jar (top, center, and bottom); the light gray curve corresponds to a control experiment in which the temperature evolution caused by the milling of pure H$_2$BDC with H$_2$O in the same experimental conditions as in Figure 1a was followed. (c) Picture obtained with the thermal imaging camera of the milling jar, highlighting the three measurement zones. The shaking direction is emphasized by the orange arrows.

Raman measurements, justifying the use of an excess amount of water in this particular example (≥16 equiv).

The system undergoes several structural transformations during the milling process, as illustrated by the shifts of specific vibration modes in the time-resolved experiment (Figure 1a). Between 800 and 900 cm^{-1} (Figure 1b, gray box), we focus on the aromatic breathing and out-of-plane (γCH) deformation region.[86−88] The signal from the starting H$_2$BDC molecule quickly shifts from 832 to 878 cm^{-1}, and after ∼8 min of milling, it evolves to 862 cm^{-1}, and finally moves to 865 cm^{-1} in the final compound. Accordingly, corresponding modifications of the ν_s(COO$^-$) band can also be easily followed between 1380 and 1480 cm^{-1}.

The products successively formed were identified as **ZTA1**, **ZTA2a**, and **ZTA2b**. Their Raman spectra and corresponding pXRD patterns are presented in Figure 1b,c in green, red, and blue, respectively. No formation of **ZTA3** occurred when using an initial Zn/BDC molar ratio of 2/1 in the milling.

Kinetic Study of the Transformations. In view of describing further the reactions occurring during the milling, the kinetic evolution of the reaction medium established by Raman spectroscopy (as determined by the integration of the previously mentioned vibration modes between 800 and 900 cm^{-1}, for example) was complemented with the thermal imaging of the milling jar (Figure 2). Simultaneous recording of temperatures at three different areas of the jar (referred to as top, center, and bottom) led to the plots displayed in Figure 2b. The inset (dashed gray area in Figure 2a) presents the first

500 s of the experiment, corresponding to the transformation of H$_2$BDC into **ZTA1** (from 832 to 878 cm^{-1}), which has a 1/1 Zn/BDC molar ratio.[40] This reaction is then followed by the introduction of an additional Zn^{2+} center in the structure and the deprotonation of two water molecules to form, after less than 8 min (<480 s) of milling, the **ZTA2a** phase (with characteristic bands at 862 and 1424 cm^{-1} in the two aforementioned regions), which has a Zn/BDC ratio of 2/1 (red curve). The reaction is probably exothermic, as shown by the increase of the temperature up to ∼40 °C (brown curve in Figure 2b). The final transformation observed in Figure 1a corresponds to the structural modification of **ZTA2a** to form the polymorph **ZTA2b** (865 and 1449 cm^{-1}), with a second increase of the temperature up to ∼47 °C (for the center temperature). Such temperature behaviors have been observed in various other systems during milling syntheses.[14,89] Figure 2b exhibits, for comparison, the milling temperature profile of a mixture of H$_2$BDC (400 mg) and H$_2$O (350 μL) (without ZnO but using similar milling conditions as in Figure 1a), allowing a difference of about 10 °C to be highlighted after ∼15 min of milling (and >15 °C after 1 h) between the Zn-BDC synthesis and the control experiment (brown *vs* gray curves).

The fact that the apparent proportion of **ZTA2a** is not null at the end of the reaction in Figure 2a (despite that its resonances have disappeared from the Raman data) can be explained by the way in which these kinetic plots were fitted here in the 860 cm^{-1} region using simple Gaussian signals
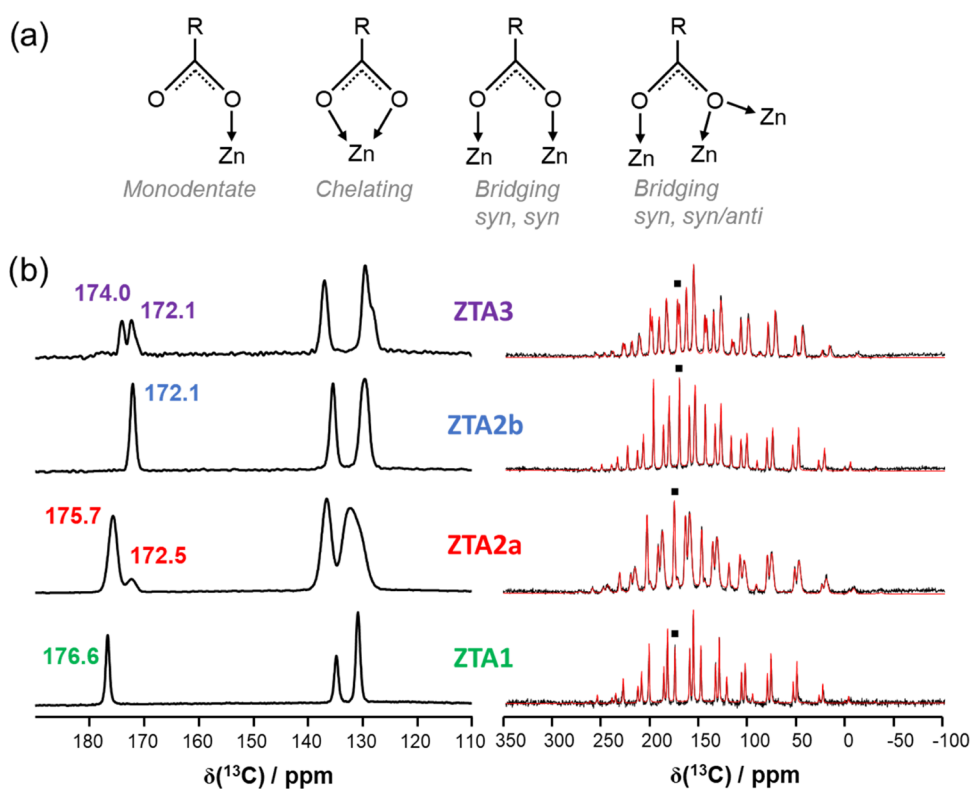
Figure 3. (a) Different possible binding modes of carboxylate ligands to Zn^{2+} ions. (b) Left: ^{13}C CP MAS NMR spectra recorded at 14.1 T with a spinning speed of 15 kHz under a regulated temperature (0 °C) (in black). Right: ^{13}C CP MAS NMR spectra recorded at 14.1 T with a spinning speed of 4.0 or 4.2 kHz under a regulated temperature (0 °C) (in black). Black-filled squares indicate the isotropic chemical shifts. The parameters used for fitting the spectra (in red) are gathered in Table 4.

centered at the different maximum frequencies of the intermediates, with intensities that were then left to freely evolve at each time point. This created ambiguities in the fitted intensities due to the closely overlapping signals of **ZTA2a** and **ZTA2b** (only ~3 cm^{-1} difference in this spectral region). More accurate kinetic plots related to the transformation of **ZTA2a** into **ZTA2b** could be obtained by fitting the 1380−1480 cm^{-1} region, where the Raman resonances of the two phases are more distinctly resolved. This is shown in Figure 2a, where the Raman signal from **ZTA2a** (red empty circles) decreases close to 0% at the end of the reaction (in line with pXRD analyses of the final compound). Because the purpose of this manuscript was not to establish a full kinetic model of the formation of these Zn-BDC phases, no attempt was made to further refine or analyze this *operando* Raman data. Yet, it is worth noting that this example illustrates the importance of having access to different regions of the Raman spectra to evaluate the quality of such kinetic fits and potentially resolve overlapping resonances. Other possibilities along this line (*e.g.* with deuterated precursors) will be discussed at the end of this article.

In the frame of this work, the clear identification of each transformation thanks to the *operando* setup involving the combined use of the Raman instrument and the thermal camera allowed each of these structures to be isolated as a pure phase for further *ex situ* structural analyses (using the optimized reaction conditions reported in Table 2). Similarly to **ZTA1**, **ZTA2a**, and **ZTA2b**, the formation of **ZTA3** could also be followed in the same fashion by *operando* Raman spectroscopy when starting from a 3/1 ratio between the ZnO and H_2BDC precursors. Hence, by choosing the adequate

stoichiometry and by stopping the milling at carefully selected times, the different Zn-BDC phases could be isolated pure, without them changing with time (see Supporting Information Figure S3). It then became conceivable to refine their structures, especially the proton positions, and to gain more insights into the terephthalate binding modes.

Refinement of the Zn-BDC Structures Using an "NMR Crystallography" Approach. When the limits of XRD methods are reached, for example, for phases that cannot be isolated as single crystals, in which some atoms cannot be positioned (*e.g.* protons) or which contain defects, ssNMR methods can be particularly useful when used in conjunction with computational modeling to gain precise information on the crystallographic structures. Such an approach, referred to as "NMR crystallography",[90,91] implies that the structures of interest possess NMR-active isotopes, which can be readily analyzed by high-resolution NMR.

In the case of Zn-BDC structures, the vicinity of the Zn^{2+} cations and more specifically the precise coordination modes of the BDC and hydroxyl ligands to Zn^{2+} are of great importance. From an NMR perspective, all atoms present in these phases have at least one NMR-active isotope, which can be studied by NMR, making them potentially attractive targets of analysis: ^1H ($I = 1/2$, 100% natural abundance), ^{13}C ($I = 1/2$, 1.07% natural abundance), ^{17}O ($I = 5/2$, 0.04% natural abundance), and ^{67}Zn ($I = 5/2$, 4.11% natural abundance). Even though ^{67}Zn NMR has recently shown promising results for providing a detailed description of zinc local environments, it is still considered as very challenging[92] because of the quadrupolar nature of zinc-67 (which can lead to very broad lines)[93] and its poor receptivity (low natural abundance and

very low resonance frequency ($\nu_L(^{67}Zn) < 10\% \nu_L(^1H)$)).[92,94] In the present work, we thus set our focus on the other three nuclei (^{13}C, ^{17}O, and ^1H) to reach a more detailed description of the binding mode of the dicarboxylate ligands and for positioning the H-atoms of the hydroxyls within the structures.

^{13}C NMR Analyses of Carboxylate Binding Modes in Zn-BDC Structures. As briefly explained earlier (*vide supra*), IR spectroscopy has been used for decades as a first approach for proposing binding modes of carboxylates to various metal ions. The difference in wavenumbers between the antisymmetric and symmetric stretching modes, defined by the parameter Δ ($=\nu_{as}(COO^-) - \nu_s(COO^-)$), has been shown to change depending on the binding mode of carboxylates, allowing, as a first approximation, the following tendency to be derived upon coordination to divalent metal ions: Δ(Chelating) $<$ Δ(Bridging) $<$ Δ(Ionic) $<$ Δ(Monodentate) (see Figure 3a).[47] However, this method can be ambiguous as Δ can be affected by other parameters, depending on the types of ligands involved and how they interact with each other within the structures. Moreover, it relies on the clear attribution of the vibration modes ($\nu_{as}(COO^-)$ and $\nu_s(COO^-)$), which actually remains uncertain in many experimental cases, due to numerous overlapping vibration bands (*e.g.*, $\nu_{as}(COO^-)$, $\nu_s(COO^-)$, $\nu(CC)$, $\beta(CCH)$, *etc.*) on the IR spectra (see Supporting Information Figure S4). In the present case, when looking at the FTIR spectrum of **ZTA2a**, the $\Delta = 210$ cm^{-1} splitting is significantly higher than expected for bridging ligands. Indeed, the other phases with bridging ligands, namely, **ZTA2b** and **ZTA3**, display values at $\Delta = 171$ and 180 cm^{-1}, respectively. Moreover, the monodentate bound ligand in **ZTA1** shows a splitting of $\Delta = 192$ cm^{-1}. Overall, this tends to show the limitations of IR spectroscopy in providing direct information on the terephthalate binding modes, but may also hint that **ZTA2a** actually exhibits more complex binding modes than suggested by the X-ray diffraction data.

Here, we decided to perform ^{13}C ssNMR analyses to obtain more information on the binding mode of the carboxylates. The ^{13}C ssNMR spectra of the four samples obtained by mechanochemistry are presented in Figure 3b (see Supporting Information Figure S5 for data on H$_2$BDC). Spectra were recorded with different spinning speeds, such as to focus on the isotropic chemical shifts (Figure 3b, left) or to derive the chemical shift anisotropy (CSA) parameters (Figure 3b, right).

Based on the reported crystal structures (see Table 1), two main binding modes were expected for the Zn-BDC compounds of interest: monodentate and bridging. For **ZTA1**, BDC ligands exhibit a monodentate configuration, and only one crystallographically inequivalent carboxylate carbon is present in the structure. For this phase, a single resonance was observed in the carboxylate region of the ^{13}C ssNMR spectrum (Figure 3b), with $\delta_{iso}(^{13}COO) = 176.6$ ppm. On the other hand, **ZTA2b** and **ZTA3** structures have different types of bridging terephthalate ligands based on the reported X-ray diffraction data. While the former clearly exhibits a single carboxylate environment ($\delta_{iso}(^{13}COO) = 172.1$ ppm), as expected from the crystal structure, the latter shows two main carboxylate resonances centered at 174.0 and 172.1 ppm (with an additional shoulder in the low-frequency area, which could perhaps be due to the presence of domains within the structure, in which terephthalate ligands exhibit very slight changes in symmetry/local environment). Finally, for the **ZTA2a** phase, while only one carbon signal was expected from the crystallographic structure, two carboxylate resonances were observed, centered at 175.7 and 172.5 ppm, and present in an ~5/1 ratio. The weaker low-frequency resonance was systematically observed for this phase (for different synthetic batches) and with the same approximate ratio. Although its ^{13}C chemical shift is relatively close to that of the H$_2$BDC precursor (173.5 *vs* 172.5 ppm), no traces of residual H$_2$BDC could be detected by IR spectroscopy in the C=O stretching region and no acidic proton signal was observed by ^1H ssNMR, meaning that this small signal cannot arise from the presence of residual H$_2$BDC (see Supporting Information Figures S6 and S7). Moreover, given that no diffraction peaks ascribable to known impurities could be detected on the X-ray diffraction pattern of **ZTA2a** (see Figure 1c and Supporting Information Figure S3), the weak resonance must correspond to systematic defects in the crystal structure, which could not be resolved nor identified by X-ray diffraction.[96]

In the literature, a few articles report ^{13}C ssNMR data for zinc-carboxylates and more specifically Zn-BDC phases.[37,49−51] In all cases, $\delta_{iso}(^{13}COO)$ was found to vary between 171.8 and 177.7 ppm. Moreover, when comparing the reported $\delta_{iso}(^{13}C)$ values of bridging carboxylates versus monodentate ones, a trend can be extracted. Indeed, the $\delta_{iso}(^{13}COO)$ values of monodentate ligands are nearly systematically more deshielded than the $\delta_{iso}(^{13}COO)$ of bridging ones. For example, Yuan et al. reported values of $\delta_{iso}(^{13}COO) = 176.7$ and 177.3 ppm for two Zn-BDC phases exhibiting monodentate binding modes (the first phase was actually the same as **ZTA1**, while the second one was Zn(BDC)(H$_2$O)), and for a Zn-BDC·DMF MOF with bridging terephthalates, they reported $\delta_{iso}(^{13}COO) = 172.7$ ppm.[50] Similarly, Julien et al. showed that the Zn(H$_2$O)$_2$(2,5-dihydroxyterephthalate) structure, which displays a monodentate configuration, exhibits a ^{13}C resonance at $\delta_{iso}(^{13}COO) = 176.0$ ppm, while MOF-74, with bridging 2,5-dihydroxyterephthalate ligands, shows signals at $\delta_{iso}(^{13}COO) = 173.2$ and 173.9 ppm (for compounds obtained by LAG using either H$_2$O or DMF, respectively).[51] Habib et al. also studied two Zn-dicarboxylate complexes, $[Zn_2(\mu_2\text{-BDC})_2(\mu_4\text{-btre})]$ and $[Zn_2(\mu_3\text{-ip})_2(\mu_2\text{-btre})(H_2O)_2]\cdot2H_2O$ (with btre = 1,2-bis(1,2,4-triazol-4-yl)ethane, ip = benzene-1,3-dicarboxylate). Each structure exhibits two distinct $\delta_{iso}(^{13}COO)$ by ^{13}C ssNMR, corresponding to two monodentate binding modes ($\delta_{iso}(^{13}COO) = 174.4$ and 173.3 ppm) for the first one, while the second complex has a bridging and a monodentate ligands ($\delta_{iso}(^{13}COO) = 174.6$ and 176.7 ppm).[49] In line with this literature survey, which shows that the $\delta_{iso}(^{13}COO)$ values for monodentate binding modes are globally deshielded compared to those for bidentate ones, it was found that the isotropic ^{13}C shifts of the carboxylates in **ZTA1**, **ZTA2b**, and **ZTA3** also appeared to follow this trend. In contrast, for **ZTA2a**, there seemed to be discrepancies with what one would have expected from the reported crystal structure, not only in the number of ^{13}C resonances (due to the additional small peak—*vide supra*) but also in the ^{13}C isotropic shift of the main resonance, which is rather high for a "bridging mode". Hence, overall, this points once again to the issues related to the X-ray data available for this phase.

To go further in the study of these, we conducted various DFT optimizations of the different structures studied here. Starting from the reported crystal structures, H-atoms were positioned (when missing). Then, keeping cell parameters constant, geometry optimizations were performed by optimizing either H positions only or all atomic positions. The H-relaxed structures did not lead to satisfactory results after the

Table 4. ^{13}C NMR Parameters of Carboxylates Extracted from Fitting Spectra Recorded at Multiple Spinning Speeds and Calculated Ones Using DFT from Optimized Structural Models of the Phases

| | | | | calculated (GIPAW-DFT)[a] | | | |
| | experimental | | | H-relaxed | fully optimized structures | | |
compound	δ_{iso} (ppm)	Ω (ppm)	κ	δ_{iso} (ppm)	δ_{iso} (ppm)	Ω (ppm)	κ
ZTA3	172.1 ± 0.3	136.9 ± 0.4	0.05 ± 0.01	167.6	172.4	130.7	0.15
	174.0 ± 0.1	139.9 ± 2.4	0.13 ± 0.01	168.0	175.6	132.3	0.31
ZTA2b	172.1 ± 0.1	137.4 ± 0.2	0.22 ± 0.01	168.0	173.4	136.2	0.15
ZTA2a	172.5 ± 0.2	140.0 ± 8.2	0.34 ± 0.15				
	175.7 ± 0.1	137.5 ± 0.4	0.20 ± 0.01	199.4	177.6	141.7	0.23
ZTA1	176.6 ± 0.1	154.7 ± 6.3	0.03 ± 0.02	176.5	181.8	146.4	0.35

[a]A systematic study of ^{13}C chemical shifts was performed in 2009 on 14 molecules (aromatics and carbohydrates) whose crystal structures have been precisely determined by neutron diffraction. This study showed that the GIPAW ^{13}C predictions are more accurate than a cluster approach, with an error on the isotropic shift of ~1 ppm.[95]

computation of NMR parameters, except for **ZTA1** (as illustrated for $\delta_{\text{iso}}(^{13}\text{COO})$ in Table 4). A more complete geometry optimization was thus needed to refine the various crystal data. Moreover, for some of the structures, it was necessary to test various initial H orientations for the hydroxyls before geometry optimization to converge toward a model that matches best the experimental data; this will be further detailed for **ZTA3** later in this article. In all cases, after these additional geometry optimization steps, the GIPAW-calculated NMR parameters for ^{13}C were found to be in relatively good agreement with the experimentally extracted values. Notably, $\delta_{\text{iso}}(^{13}\text{COO})_{\text{calc}}$ of the monodentate **ZTA1** ligand was the most deshielded of the series, with a calculated ^{13}C chemical shift at 181.8 ppm, while $\delta_{\text{iso}}(^{13}\text{COO})_{\text{calc}}$ from bridging ligands were ~6−10 ppm lower in frequency. Moreover, the calculated chemical shift anisotropy (CSA) parameters after full geometry optimization were also found to be in relatively good agreement with the experimental values, as further discussed below. These DFT-optimized structures can thus be considered as more reliable structural models of the four Zn-BDC phases studied here (see Supporting Information Figure S8).

Following this, the structures after full relaxation of atom positions were analyzed in detail, and relationships between calculated ^{13}C NMR parameters and local environments of the carboxylates (in the geometry-optimized structures) were looked into (see Supporting Information Figure S9). Significant structural modifications were observed upon full geometry optimization of some of the phases. For example, the **ZTA3** crystallographic structure was found to undergo various changes, the major one being the modification of one zinc coordination from a 5-fold O-coordination environment (Zn2 in Table 1) to a 4-fold one. In the case of **ZTA2a**, significant variations in the carboxylate binding modes were observed during the relaxation of all atom positions, which can explain the ~20 ppm decrease in the $\delta_{\text{iso}}(^{13}\text{COO})_{\text{calc}}$ value between H-relaxed and fully relaxed models (see Table 4). Still for this phase, the calculated ^{13}C NMR parameters were found to be in good agreement with those of the most intense ^{13}C resonance (i.e., $\delta_{\text{iso}}(^{13}\text{COO})_{\text{exp}}$ = 176.4 ppm vs $\delta_{\text{iso}}(^{13}\text{COO})_{\text{calc}}$ = 175.7 ppm), again with a relatively high chemical shift compared to what one may have expected for bridging carboxylates. Yet, when looking more closely at the local environment of the carboxylate after full geometry optimization, the coordination mode was actually found to be closer to a bridging *syn,syn/anti* configuration (see Figure 3a) than to monodentate or bridging *syn,syn* ones. In this configuration, one of the $d_{\text{Zn}\cdots\text{O}}$ distances

was found to be shorter (in the range of $d_{\text{Zn}\cdots\text{O}}$ for *syn,syn* bridging modes, i.e., ~2.0 Å) than the two others (which were measured between 2.2 and 2.3 Å). This may be one of the reasons for the higher ^{13}C shift of this phase, compared to bridging modes involving only shorter Zn$\cdots$O bonds.

To go even further in trying to relate ^{13}C NMR parameters to structural/geometric information about carboxylate bindings, the calculated data collected from the numerous geometry optimizations on Zn-BDC phases (especially the **ZTA3** structure) were compiled. The most obvious trend we found was between the $\delta_{\text{iso}}(^{13}\text{COO})_{\text{calc}}$ and the longest C−O distance of the carboxylate, $(d_{\text{C−O}})_l$: the highest chemical shifts are clearly related to structures with the longest C−O distances $(d_{\text{C−O}})_l$ (see Supporting Information Figure S9). *A contrario*, no unambiguous relationship relating $\delta_{\text{iso}}(^{13}\text{COO})$ and the type of carboxylate coordination could be extracted, showing that this parameter actually depends on several factors.

As ^{13}C CSA parameters can also be used to describe the local environment of carbon atoms, these were extracted from the experimental ^{13}C NMR spectra recorded at two different spinning speeds (Table 4). The most noticeable difference between compounds was in the CSA span (Ω), which was found to be experimentally higher by approximately 15−20 ppm for **ZTA1** (monodentate binding) than for the carboxylates of the three other compounds (155 vs 135−140 ppm, respectively) (see Supporting Information Figure S10 and Table S1). DFT-calculated values of spans also followed the observed trend, the highest value being for **ZTA1**, with, however, the calculated span of **ZTA2a** now only about 5 ppm lower than that calculated for **ZTA1**. Using the data library obtained by optimizing the Zn-BDC structures and also different structural models of **ZTA3**, attempts were made to relate the various CSA parameters stemming from the calculations to carboxylate binding modes. Here, a general trend was also observed between the longest C−O distance $(d_{\text{C−O}})_l$ and Ω_{calc} (see Supporting Information Figure S11), but no direct relationship with the carboxylate coordination.

Overall, although hints about carboxylate local environments could be derived from ^{13}C ssNMR spectra, no complete insight into the carboxylate coordination mode could be obtained. Hence, we then considered analyzing local environments of oxygen atoms because they are directly coordinated to the Zn^{2+} ions in the Zn-BDC structures and may help gain insights into the various binding modes.

^{17}O NMR Analyses of Carboxylate and Hydroxyl Binding Modes in Zn-BDC Structures. With the aim of directly probing the binding modes of the terephthalate ligands by ^{17}O ssNMR,
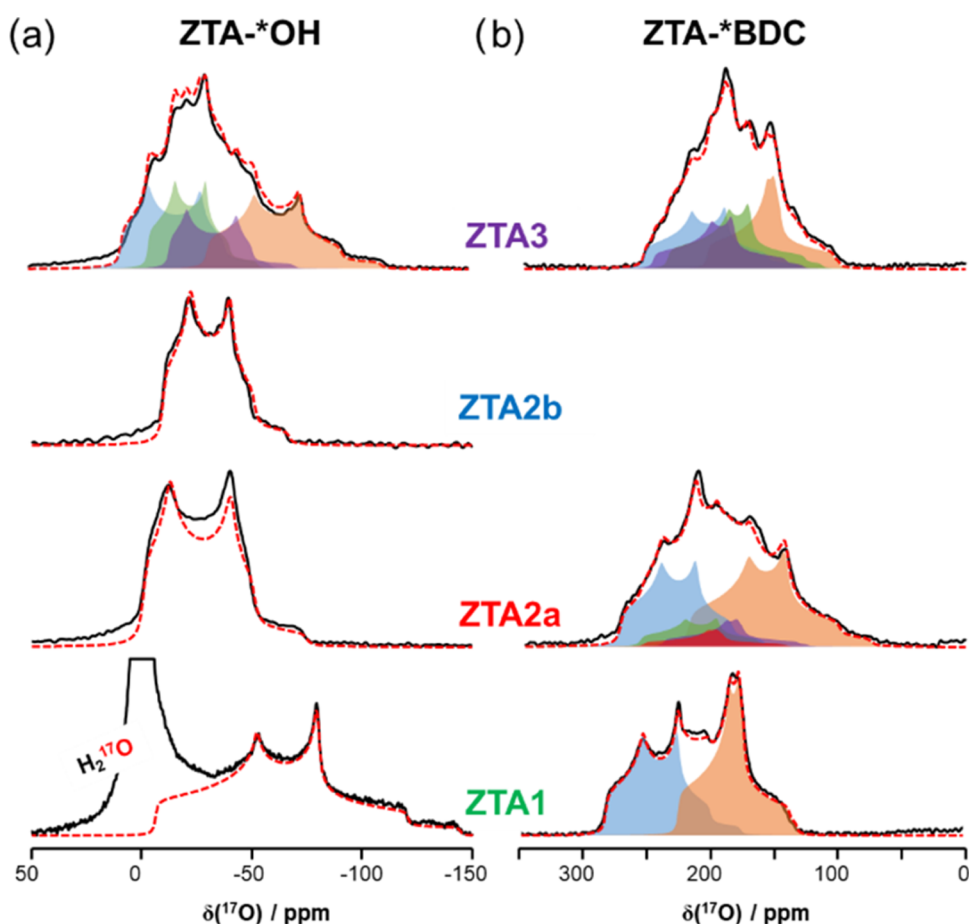
Figure 4. ^{17}O MAS NMR spectra of ^{17}O-labeled Zn-BDC compounds prepared by mechanochemistry, $B_0 = 14.1$ T, $\nu_{rot} = 18$ kHz, and $T = 0$ °C. (a) **ZTA-*OH** samples corresponding to the enrichment of the hydroxyl/water groups. (b) **ZTA-*BDC** samples corresponding to the enrichment of the BDC moiety. For all spectra, experimental spectra are in black, and the red dotted line corresponds to the results of the fitting process.

^{17}O-labeled terephthalic acid was used as a starting material to prepare Zn-BDC phases enriched on the carboxylate groups. Concerning the bridging hydroxyls, a direct enrichment during the mechanochemical synthesis of the Zn-BDC phases was envisaged using ^{17}O-enriched water as a starting reactant (instead of normal water).

Both labeling strategies were tested for each compound (**ZTA1, 2a, 2b,** and **3**) to isolate Zn-BDC phases selectively enriched on the carboxylates or on the hydroxyls/water and then perform high-resolution NMR spectroscopy. All samples could be prepared by mechanochemistry, with selective enrichment on the carboxylate part (phases noted **ZTA-*BDC**) or the hydroxyl/water part (phases noted **ZTA-*OH**), with the exception of **ZTA2b**, for which the carboxylate-enriched phase (**ZTA2b-*BDC**) could not be obtained with sufficient purity to be analyzed by ^{17}O ssNMR. In total, six different enriched samples were thus isolated with good purity, using the BM synthetic procedure developed above thanks to the *operando* Raman setup. In all cases, preliminary evidence of the success of the enrichment could be assessed by FTIR, with the slight shifts of vibration modes such as $\nu_{as}(COO^-)$ and $\nu_s(COO^-)$ (see Supporting Information Figure S4c). The corresponding 1D ^{17}O MAS NMR spectra are presented in Figure 4, which could all be recorded with good sensitivity in just a few hours.

Because oxygen-17 is a quadrupolar nucleus, the NMR resonances recorded on the 1D spectra show characteristic

second-order quadrupolar line shapes. To extract the ^{17}O NMR parameters associated with each oxygen environment (δ_{iso}, C_Q, and η_Q), spectra were fitted at multiple fields (see Supporting Information Figures S14–S17), since the second-order quadrupolar broadening decreases as the magnetic field increases. Moreover, additional 2D high-resolution MQMAS (multiple-quantum MAS) experiments were also recorded for some of the phases, allowing the fits to be further refined (see Supporting Information Figures S12 and S13).

Regarding the **ZTA-*OH** phases labeled on the hydroxyl/water positions, the NMR spectra were found to be generally easier to analyze (Figure 4a). Only one *OH site was observed for both **ZTA2a-*OH** and **ZTA2b-*OH**, as expected from the published crystal structures. In contrast, **ZTA3-*OH** was found to exhibit a more complex line shape consisting of several inequivalent sites (Figure 4a). These were resolved using a ^{17}O MQMAS NMR experiment (see Supporting Information Figure S12). Moreover, the OH network of this compound was further investigated through a $^1H-^{17}O$ dipolar correlation experiment, as detailed below (see Figure 5).

The D-HMQC experiment allows $^1H\cdots^{17}O$ proximities to be probed and turned out to be highly useful to help position the hydroxyl protons (which were absent from the initial X-ray diffraction data). Here, a short recoupling time was used ($\tau_{rec} = 100$ μs) to observe the shortest $O\cdots H$ contacts (*i.e.*, the $O-H$ bonds). In these conditions, no correlation between hydroxyl oxygen atoms and aromatic protons was observed (blue-
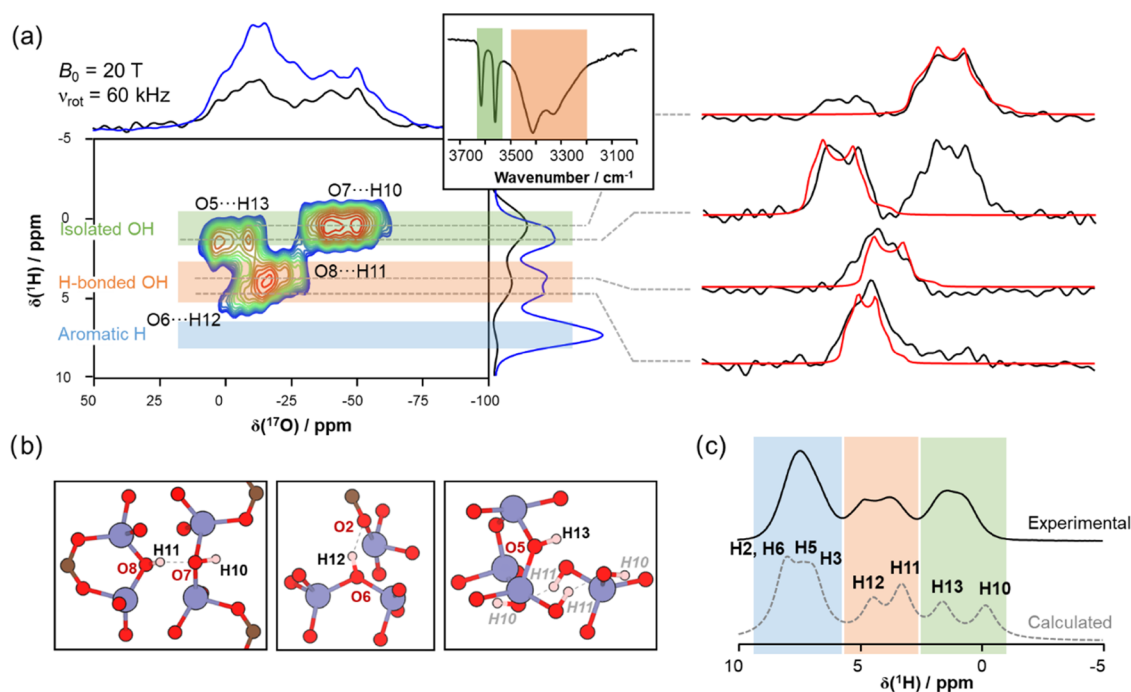
Figure 5. (a) $^1H-^{17}O$ D-HMQC of **ZTA3-*OH** recorded at 20.0 T under a spinning speed of 60 kHz. The ^{17}O and ^1H 1D spectra recorded in the same condition as the D-HMQC are shown in blue. Extracted slices (in black) are fitted (red lines) with the experimental parameters presented in Table 5. The inset displays the FTIR spectrum centered on the OH stretching region. H-bonded OH groups are highlighted in orange, and isolated OH groups are shown in green. (b) Close-up views of the DFT-optimized **ZTA3** structure of the different hydroxyl environments; color code: brown for carbon, red for oxygen, light pink for hydrogen, and purple for zinc. (c) Comparison of experimental ^1H MAS spectrum (recorded at B_0 = 20.0 T and ν_{rot} = 60 kHz, in black) and simulated spectrum from calculated ^1H NMR parameters in dotted gray.

Table 5. ^{17}O ssNMR Parameters Extracted from Experimental Spectra (Figure 4) Recorded at Multiple Magnetic Fields and Calculated Using DFT from Structural Models of the Phases

		experimental				calculated		
enrichment	compound	$\delta_{iso}(^{17}O)$ (ppm)	$C_Q{}^a$ (MHz)	η_Q	Int (%)	$\delta_{iso}(^{17}O)$ (ppm)	C_Q (MHz)	η_Q
*OH	ZTA3	12.8 ± 0.6	5.59 ± 0.02	0.30 ± 0.02	27.2	6.1	−7.88	0.64
		−1.9 ± 0.1	4.71 ± 0.04	0.43 ± 0.10	17.9	3.7	6.81	0.98
		−8.5 ± 0.1	5.22 ± 0.01	0.23 ± 0.02	23.6	0.4	−4.31	0.53
		−27.9 ± 0.2	5.92 ± 0.02	0.47 ± 0.01	31.3	−27.3	−7.98	0.51
	ZTA2b	−5.6 ± 0.4	5.10 ± 0.10	0.36 ± 0.01	100	−9.9	−5.92	0.33
	ZTA2a	5.5 ± 1.3	5.90 ± 0.12	0.25 ± 0.02	100	1.8	−6.89	0.34
	ZTA1	−3.2 ± 3.0	7.66 ± 0.20	0.61 ± 0.04	100	−15.8	9.32	0.49
*BDC	ZTA3	258.4 ± 0.1	7.23 ± 0.01	0.56 ± 0.01	28.5	276.3	7.73	0.80
		249.0 ± 0.7	6.97 ± 0.02	0.74 ± 0.03	25.3	273.4	7.93	0.84
		237.3 ± 0.5	7.06 ± 0.01	0.75 ± 0.06	19.9	254.7	−6.77	0.97
		205.2 ± 0.8	6.39 ± 0.05	0.90 ± 0.10	26.3	210.2	−7.26	0.63
	ZTA2a	278.3 ± 1.6	7.07 ± 0.10	0.51 ± 0.11	32.3	298.1	7.37	0.69
		261.3 ± 1.0	7.04 ± 0.02	0.56 ± 0.13	10.5			
		255.7 ± 1.5	6.70 ± 0.21	0.88 ± 0.12	5.2			
		240.3 ± 5.3	6.74 ± 0.30	0.85 ± 0.15	8.7			
		223.0 ± 1.1	7.85 ± 0.05	0.60 ± 0.08	43.3	253.0	8.79	0.62
	ZTA1	286.6 ± 1.3	6.90 ± 0.05	0.46 ± 0.02	50.9	320.6	7.46	0.69
		221.7 ± 2.1	5.83 ± 0.49	0.85 ± 0.01	49.1	251.3	−6.71	0.67

^{a}Experimental C_Q values are given in absolute values.

shaded zone) but four environments could be resolved for the hydroxyls, one per inequivalent OH, in line with the published crystal structure (three being μ_3-OH and one being μ_2-OH). More interestingly, when looking at the FTIR spectrum of **ZTA3** (see the inset of Figure 5a), four environments of the hydroxyls could also be detected and separated into two groups: two for isolated OH species (green-shaded zone) and

two for OH species involved in H-bonding (orange-shaded zone). A similar distinction can be made using the D-HMQC data. Indeed, the most shielded oxygen site ($\delta_{iso}(^{17}O)$ = −27.9 ppm) and the most deshielded one ($\delta_{iso}(^{17}O)$ = 12.8 ppm) are correlated to ^1H resonances with low chemical shift (close to 0 ppm), such ^1H shifts being characteristic of isolated OH groups (zone shaded in green).[97,98] On the other hand, the
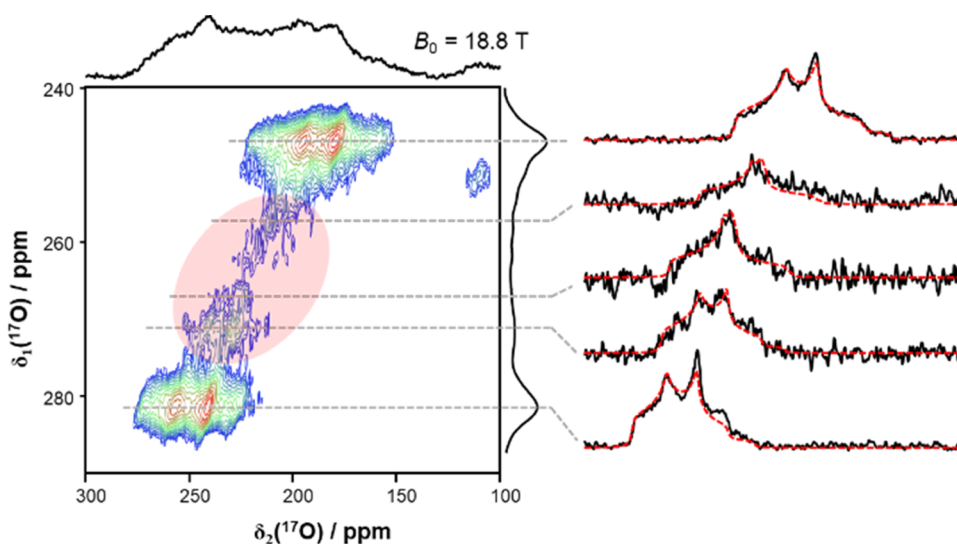
Figure 6. ^{17}O MQMAS spectrum of **ZTA2a-*BDC** recorded at $B_0 = 18.8$ T under $\nu_{rot} = 16$ kHz. Extracted slices (in black) are fitted (red dotted lines) with experimental parameters presented in Table 5. The red-shaded circle enlightens some of the additional oxygen sites corresponding to structural defects.

two remaining OH sites are correlated to ^{1}H resonances, with $\delta_{iso}(^{1}H)$ close to 5 ppm, implying that they are involved in hydrogen bonds (orange-shaded zone).[87−99]

Using these high-resolution $^{1}H-^{17}O$ experiments as a guideline, different configurations were tested to position the four hydroxyl hydrogens in the **ZTA3** structure, which were then geometry-optimized by DFT. The resulting GIPAW-DFT-computed ^{1}H ssNMR spectrum of the best model is highly comparable to the high spinning speed ^{1}H NMR spectrum (Figure 5c). The resulting refined **ZTA3** structure exhibits two isolated hydroxyls: one (O5-H13) is shared between Zn3−Zn2−Zn3 (μ_3-OH), while the second one (O7−H10) is located between Zn1−Zn2 (μ_2-OH); both display a low $\delta_{iso}(^{1}H)$ chemical shift (1.34 and 0.80 ppm, respectively). In contrast, the hydroxyl protons denoted H11 and H12 have a higher chemical shift, indicative of the presence of a hydrogen-bonding network, as can be seen in the geometry-optimized structure (see Figure 5b): the H11···O7 and H12···O2 distances were found to be only ~1.7 Å.

Generally speaking, the calculated ^{17}O NMR parameters were found to be in satisfactory agreement with those extracted from experimental data. The overestimation of C_Q, often observed in Table 5, is consistent with what has been recently reported in the ^{17}O NMR literature on MOFs.[59,100] However, unlike the calculated ^{13}C NMR parameters, no clear trend between ^{17}O NMR parameters and structural geometric parameters (d_{C-O}, $d_{Zn\cdots O}$, $\theta_{Zn\cdots O-C}$...) could be derived (see Supporting Information Figures S18 and S19). This is probably due to the multifactorial dependence between the ^{17}O NMR parameters and the local environment and geometry around the oxygen in these structures.

Concerning the phases enriched on the carboxylates, the experimental $\delta_{iso}(^{17}O)$ arising from the BDC* ligands of the different structures were found to span between 205.2 and 286.6 ppm (see Figure 4b). **ZTA1-*BDC** exhibits two clear inequivalent oxygen resonances, as expected from the crystal structure. On the contrary, **ZTA2a-*BDC** and **ZTA3-*BDC** gave more complex signatures due to the presence of several overlapping resonances. The ^{17}O MAS NMR spectra of **ZTA3-*BDC** could, for example, be fitted considering the presence of

four different ^{17}O signals, as expected from the crystal structure and resolved with the MQMAS experiments (see Supporting Information S12). Concerning the **ZTA2a-*BDC** phase, only two carboxylate oxygen resonances were expected according to the reported crystal structure. However, it was not possible to obtain a satisfactorily simulated spectrum with only two signals. This result supports the observation made previously by ^{13}C NMR for **ZTA2a**, where an additional ^{13}C carboxylate resonance of weak intensity was detected at 172.5 ppm (see Figure 3b).

To learn more about the minor carboxylate environments in **ZTA2a**, the ^{17}O MQMAS spectrum of **ZTA2a-*BDC** was recorded (Figure 6). The two most intense resonances, which are centered at $\delta_{iso}(^{17}O) = 278.3$ and 223.0 ppm, belong to the main carboxylate group (i.e., with the ^{13}C signal at 175.7 ppm). Yet, several signals of weaker intensity can also be observed (red-shaded circle), corresponding to multiple and slightly different carboxylate local environments (such regions of signals with lower intensity have been observed on two different batches of **ZTA2a-*BDC** with two different NMR spectrometers). Three examples of these additional oxygen environments were extracted from this area for further study (Figure 6, right).

Despite their low signal-to-noise ratio, the signals from the three different slices could be tentatively fitted using quadrupolar line shapes, suggesting that they correspond to carboxylate oxygens in a relatively well-ordered local environment. Using the NMR parameters derived from the different ^{17}O environments resolved by MQMAS, it was then possible to propose a fit of the ^{17}O NMR spectra of **ZTA2a-*BDC** in the carboxylate region (see Figure 4b and Table 5). However, it should be kept in mind that additional weak-intensity carboxylate resonances may also be overlapping with the two main resonances (which remained unresolved at this stage). Interestingly, the ^{17}O NMR data also show that the main resonances for **ZTA2a-*BDC** ($\delta_{iso}(^{17}O) = 278.3$ and 223.0 ppm) are relatively close in shift to those of **ZTA1-*BDC** ($\delta_{iso}(^{17}O) = 286.6$ and 221.7 ppm), further underscoring the similarities between ^{17}O ssNMR and ^{13}C ssNMR parameters ($\delta_{iso}(^{17}O)$, $\delta_{iso}(^{13}COO)$, and ^{13}C CSA) for the two different
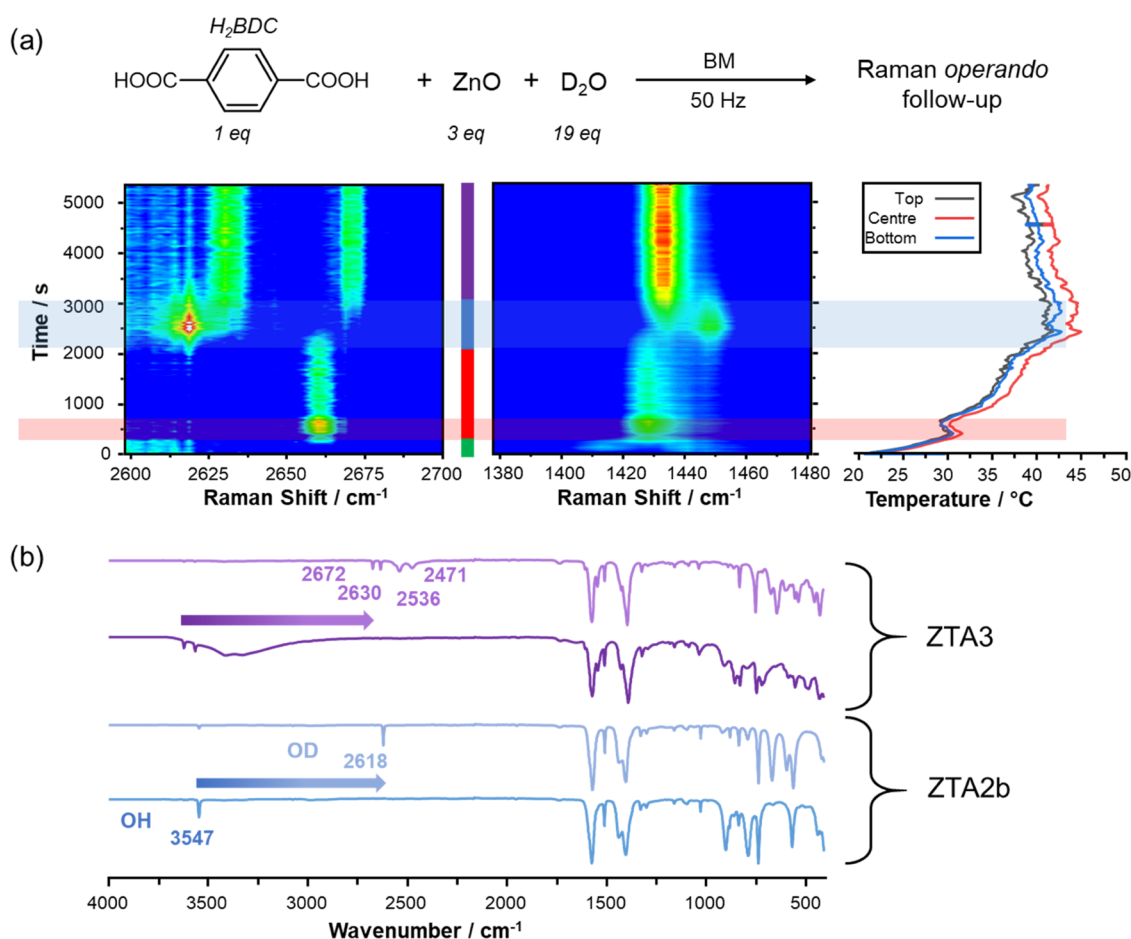
Figure 7. (a) Top: starting compounds used for the *operando* experiment with their respective equivalents. Bottom: time-resolved *operando* Raman spectra of two selected areas: 2600−2700 cm^{-1} range on the left and 1380−1480 cm^{-1} range on the right, following the Raman spectroscopy convention for displaying the data (high wavenumbers on the right). The graph on the far right corresponds to the temperature measurement recorded using the thermal imaging camera. (b) Experimental *ex situ* FTIR spectra of **ZTA2b** (in blue), **ZTA2b-OD** (in light blue), **ZTA3** (in purple), and **ZTA3-OD** (in light purple), following the FTIR spectroscopy convention for displaying the data (high wavenumbers on the left).

binding modes, *i.e.*, *syn,syn/anti* bridging (**ZTA2a**) and monodentate (**ZTA1**). Regarding the weaker signals (red circle in Figure 6), they are likely to arise from the presence of the systematic defects inside the crystallographic structure, as already hinted from the ^{13}C NMR data.

Thanks to the selective ^{17}O-labeling of the various Zn-BDC compounds by BM, it was possible to gain novel insights into the local environment of the oxygen-containing ligands, as well as refine one of the crystallographic structures (**ZTA3**) by DFT calculations. Although no straightforward trend relating ^{17}O NMR parameters to carboxylate binding modes could be derived, most probably because of the influence of several geometrical features (Zn···O and O−C distances, bond angles, positioning of neighboring ligands, *etc.*), high-resolution ^{17}O ssNMR spectroscopy, in conjunction with DFT calculations and GIPAW calculations of NMR parameters, clearly appears as a crucial asset to help confirm the structural models of these types of MOFs. In particular, they will be useful in the future to help elucidate the nature of the defect sites in **ZTA2a** in an NMR crystallography type of approach.[101]

Outlook: Isotope Labeling for Simplified In Situ Observations of Evolutions in the Reaction Media. Because structural rearrangements occur around the water molecules/hydroxyls during the Zn-BDC transformations described above, being able to follow this by Raman spectroscopy appeared to us as an

important goal to increase our insight into the transformations taking place. Unfortunately, it was not possible to follow the evolution of the O−H stretching modes upon synthesis by BM with our Raman setup because it only allowed spectra to be recorded from 220 to 3120 cm^{-1}, while ν(OH) bands most often appears at higher wavenumbers.[102−104]

To circumvent this issue, we thus decided to perform isotope labeling of Zn-BDC phases using deuterium oxide rather than normal water as a starting material in the syntheses. In doing so, the stretching modes arising from −OH groups would correspond to -OD groups, which can be observed between 2400 and 2800 cm^{-1}. Figure 7 presents as an example the result of a synthesis followed by *operando* Raman spectroscopy and performed using an initial Zn/BDC ratio of 3/1 (*i.e.*, one additional equivalent of ZnO compared to the experiment presented in Figure 1) and D$_2$O instead of H$_2$O. The corresponding temperature measurement through the thermal imaging camera is placed on the side of the Raman spectra (Figure 7a), and the focus of the Raman data is set in the zone between 2600 and 2700 cm^{-1}, where O−D stretching vibrations appear.

With the starting experimental conditions used here, it is expected to obtain a different final product (*i.e.*, **ZTA3**) compared to the experiment presented in Figure 1 (final product was **ZTA2b**). The formation and progressive trans-
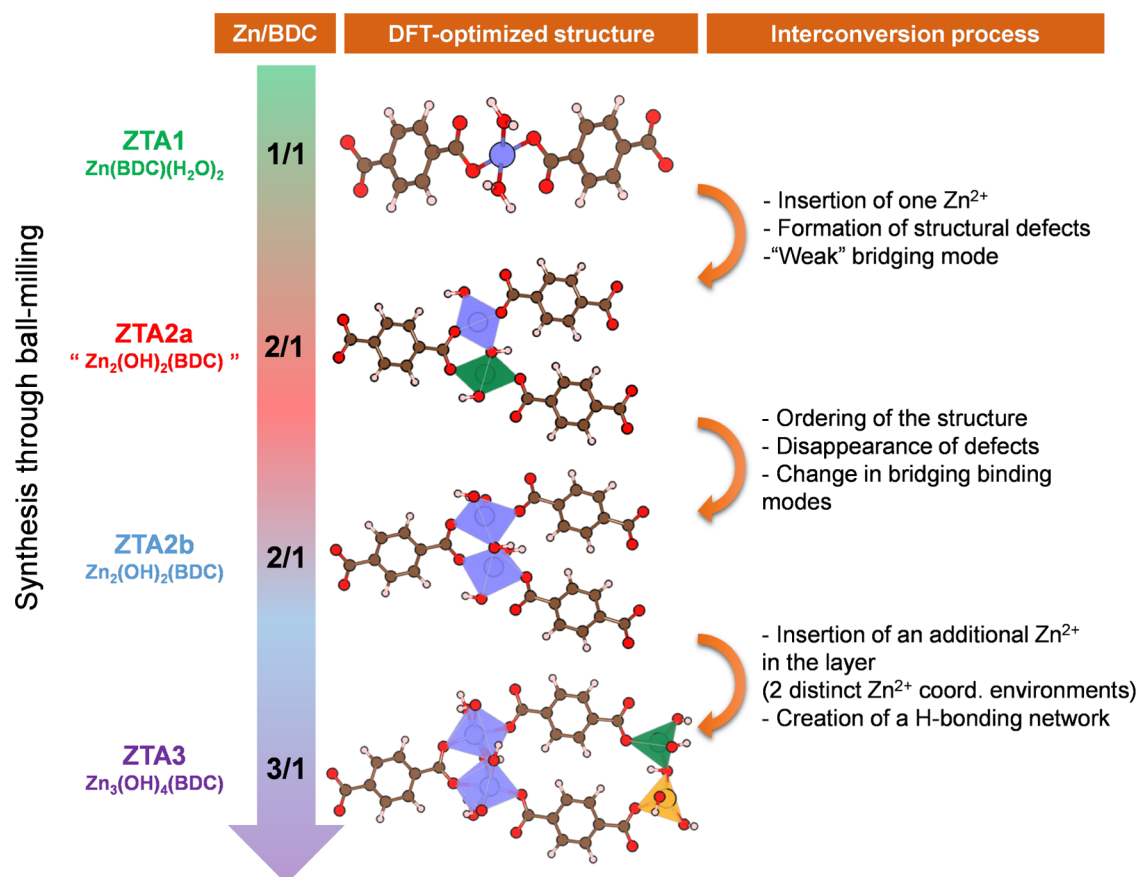
Figure 8. Summary of the structural evolution of the Zn-BDC compounds presented in this article upon milling synthesis. The molecular schemes arise from the DFT-optimized structures obtained in this article.

formation of the intermediates into **ZTA3** are indeed noticeable through the change in temperature, as well as the modifications of the Raman spectra. It should be noted that no signal from **ZTA1** was observed in the 2600−2700 cm^{-1} area (Figure 7) because of the lack of isolated OH environments in this phase, the water molecules being involved in hydrogen bonds. The broad signal arising from these water molecules is indeed too weak to be detected during the *operando* Raman experiment. Hence, in the 2600−2700 cm^{-1} range, when working with a 3/1 Zn/BDC ratio in D_2O, we observed first the formation of the **ZTA2a-OD**, through the presence of the $\nu(OD)$ band (2660 cm^{-1}). As with the synthesis presented in Figure 1, it then transforms into the **ZTA2b-OD** structure (2618 cm^{-1}). Then, the excess of zinc oxide allows the formation of the **ZTA3-OD** compound as the final form ($\nu(OD)$ = 2630 and 2671 cm^{-1}). This final phase has a Zn/BDC stoichiometry of 3/1, consistent with the one between the reagents introduced in the jar. The transformation from H_2BDC to **ZTA3** can also be observed looking at $\nu_s(COO^-)$ band between 1380 and 1480 cm^{-1}, the only difference with Figure 1 being the final transformation into the **ZTA3** phase (**ZTA3-OD** here) in the later synthesis. It is worth noting that we were able to observe the two distinct sharp O−D bands in the final compound, corresponding to the expected two isolated hydroxyls (Zn−O(H)−Zn).

The interest of using deuterated precursors for *operando* Raman mechanochemistry was further demonstrated here, using ring-d_4 terephthalic acid as a starting reagent. In doing so, the $\nu(CH)$ Raman signals become $\nu(CD)$ signals, which, in

the case of **ZTA1**, for example, corresponds to a shift of the stretching vibrations from 3064 and 3105 cm^{-1} to 2287 and 2321 cm^{-1} (see Supporting Information Figure S20).[105] Therefore, isotope labeling by deuteration can be seen as a way of shifting Raman vibrations in an area of the spectrum where no signal from the jar is expected, allowing a more straightforward observation of the evolving vibration modes as well as an easier postsynthesis data treatment. Both methods, using D_2O or d_4-BDC, can also be combined to study the change of kinetics for such reactions. Overall, this demonstrates, beyond the study of reaction mechanisms in ball-milling,[106] how isotopic labeling by deuteration can be particularly useful also for following the kinetics in mechanochemical reactions by shifting vibration bands into regions where they become detectable (*e.g.*, OD *vs* OH) and/or to avoid overlaps with other vibration frequencies (including from the jar). Such strategies may also turn out to be particularly valuable to refine kinetic data, which may be ambiguous in other regions (as highlighted at the beginning of this manuscript) and thereby help elucidate complex mechanochemical reactions.

■ CONCLUSIONS

In this contribution, we have performed the first in-depth study of the formation and structure of four coordination polymers involving Zn^{2+} cations and terephthalate ligands, noted **ZTA1**, **ZTA2a**, **ZTA2b**, and **ZTA3**. Although each of these phases had been previously reported independently (for instance, as part of investigations aiming at studying the formation of the

well-known MOF-5 structure), the details of their structure, and in the case of **ZTA2a**, the possibility to isolate it as phase-pure, were missing. Here, it is shown for the first time how using mechanochemistry, in conjunction with *operando* Raman spectroscopy and thermal imaging, the evolution of the reaction medium could be followed. Each of the phases could be isolated as pure, either by adapting the stoichiometry of the Zn and BDC precursors involved in the milling, or by stopping the milling synthesis at a specific time point based on knowledge of the kinetics of the reactions. The study of the formation of **ZTA3** by mechanochemistry was shown to proceed through the successive formation of the **ZTA1**, **ZTA2a**, and **ZTA2b** intermediates (see Figure 8).

For each of the phases, an NMR crystallography approach was then used, combining high-resolution NMR spectroscopy with *ab initio* DFT calculations of NMR parameters, to help refine the crystal structures, as much information was lacking in the crystallographic data available to date. Regarding ^{13}C ssNMR, a systematically lower $\delta_{iso}(^{13}COO)$ was observed for *syn,syn* bridging ligands as opposed to monodentate and weaker *syn,syn/anti* bridging modes (~4 ppm difference in shifts). Moreover, $\delta_{iso}(^{13}COO)$ and the CSA span (Ω) parameter were found to correlate reasonably well with the longest C−O distance of the carboxylate, making the measurement of these parameters valuable for extracting structural information in future studies of other unknown Zn-terephthalate coordination networks. Furthermore, the ^{13}C ssNMR study allowed an additional carboxylate resonance to be detected for the **ZTA2a** compound reflecting the likely presence of "defect" in that structure.

Regarding ^{17}O ssNMR, the key point to highlight is that using the protocols developed here by mechanochemistry, it was possible to produce, at low cost, selectively ^{17}O-labeled phases in high yield, with either enriched hydroxyls (Zn−O*(H)−Zn) or enriched carboxylates (CO*O*−Zn) and no isotopic scrambling during the milling (as shown in Figures S14 and S15). Such selective labeling was possible because reactions were performed here by BM under "ambient" temperature and pressure, and in short times (less than 3 h). Moreover, it is important to highlight that the syntheses of these ^{17}O-enriched compounds would have been far too expensive if not for the BM procedures optimized through the use of real-time monitoring Raman spectroscopy. Indeed, the extent of enriched H$_2$O* employed here was very low (for **ZTA-*OH**, ~45 μL for ~300 mg of sample recovered and ~20 μL for ~110 mg of sample recovered for **ZTA-*BDC**) and could not have been matched for syntheses carried out using the hydrothermal or microwave procedures proposed so far to prepare such compounds. Thanks to this isotopic labeling, high-resolution ^{17}O ssNMR spectra could be recorded for each of the phases in just a few hours, allowing different carboxylate oxygen and hydroxyl environments to be resolved. This enabled, for example, a very precise positioning of hydroxyl hydrogens in the case of the **ZTA3** phase. Regarding terephthalate ligands, however, no straightforward correlation between ^{17}O NMR parameters and geometric features around the carboxylate oxygens could be derived, showing that the ^{17}O data in these phases are very sensitive to the local environment of oxygen and depend on many different factors (*e.g.*, bond distances, angles). This implies that combined experimental−computational approaches involving various NMR-active nuclei, including ^{17}O, are a very valuable tool for validating

structural models (and notably carboxylate binding modes) of these materials.

Among the four phases studied, the **ZTA2a** compound was proven to present a more complex structure than the one reported, with the probable presence of "defect" sites, as evidenced from both ^{13}C and ^{17}O ssNMR analyses. The information derived from these spectra can serve as the basis for proposing structural models of these defects, which can then be validated using DFT calculations of NMR parameters. More generally speaking, considering the increasing number of studies on MOF structures, which highlight the importance of further refining structural data (beyond what is possible by using powder X-ray diffraction) and to establish the nature and role of defects on reactivity, the possibility of using approaches such as the ones proposed herein, including selective ^{17}O isotopic enrichment, appears very valuable.

Lastly, through the study of the mechanochemical formation of the four Zn-BDC phases using *operando* Raman spectroscopy, we also demonstrate here for the first time how the use of deuterated precursors can be useful to help follow the course of the reactions by enabling the observation of specific vibration modes (*e.g.*, ν(OD) and/or ν(CD)) and thereby avoiding cutoff of high wavenumbers of the ν(OH) and/or ν(CH) modes due to instrumentation, and/or avoiding their overlap with signals arising from the milling jar in the Raman spectra. We foresee that on a more general perspective, the study of deuterated compounds in *operando* Raman investigations by BM will be particularly useful to refine the understanding of the reactions occurring in the jars and may enable the more straightforward investigation and optimization of reactions, which not only concern the formation of MOFs but may actually more specifically involve the formation of C−D (instead of C−H) bonds, as it is the case in reduction reactions in organic chemistry.

■ ASSOCIATED CONTENT

ⓢ Supporting Information

The Supporting Information is available free of charge at https://pubs.acs.org/doi/10.1021/acs.chemmater.1c04132.

> Experimental details and additional supporting tables and figures: selected ssNMR data (^{1}H, ^{13}C, and ^{17}O NMR spectra, together with their fits); pXRD, FTIR, and Raman data; and graphical plots related to DFT calculations and structural parameters (PDF)

■ AUTHOR INFORMATION

Corresponding Authors

César Leroy − *ICGM, Univ Montpellier, CNRS, ENSCM, 34293 Montpellier, France*; Email: cesar.leroy@umontpellier.fr

Danielle Laurencin − *ICGM, Univ Montpellier, CNRS, ENSCM, 34293 Montpellier, France*; ⓞ orcid.org/0000-0002-7445-0528; Email: danielle.laurencin@umontpellier.fr

Authors

Thomas-Xavier Métro − *IBMM, Univ Montpellier, CNRS, ENSCM, 34293 Montpellier, France*; ⓞ orcid.org/0000-0003-2280-3595

Ivan Hung − *National High Magnetic Laboratory (NHMFL), Tallahassee, Florida 32310-3706, United States*; ⓞ orcid.org/0000-0001-8916-739X

Zhehong Gan − *National High Magnetic Laboratory (NHMFL), Tallahassee, Florida 32310-3706, United States;* ⦿ orcid.org/0000-0002-9855-5113

Christel Gervais − *Laboratoire de Chimie de la Matière Condensée de Paris (LCMCP), UMR 7574, Sorbonne Université, CNRS, F-75005 Paris, France;* ⦿ orcid.org/0000-0001-7450-1738

Complete contact information is available at:
https://pubs.acs.org/10.1021/acs.chemmater.1c04132

Author Contributions

The project was conducted by C.L. in close interaction with D.L., T.-X.M., and C.G. T.-X.M., C.L., and D.L. developed together the *operando* Raman spectroscopy setup coupled to mechanochemistry. C.L. performed all BM syntheses, all characterizations by IR, Raman, and pXRD, and the vast majority of ssNMR analyses. I.H. and Z.G. performed part of the high-field ^{17}O NMR experiments reported herein (MagLab). C.G. carried out the computational simulations and GIPAW-DFT calculations. C.L. performed the data analyses and prepared all figures and tables. C.L. and D.L. wrote the initial draft of the manuscript. All authors discussed the results and contributed to the final preparation of the manuscript.

Notes

The authors declare no competing financial interest.

■ REFERENCES

(1) Friščić, T.; Mottillo, C.; Titi, H. M. Mechanochemistry for Synthesis. *Angew. Chem., Int. Ed.* **2020**, *59*, 1018−1029.

(2) Boulineau, S.; Courty, M.; Tarascon, J.-M.; Viallet, V. Mechanochemical Synthesis of Li-Argyrodite Li$_6$PS$_5$X (X = Cl, Br, I) as Sulfur-Based Solid Electrolytes for All Solid State Batteries Application. *Solid State Ionics* **2012**, *221*, 1−5.

(3) Do, J.-L.; Friščić, T. Mechanochemistry: A Force of Synthesis. *ACS Cent. Sci.* **2017**, *3*, 13−19.

(4) Tan, D.; García, F. Main Group Mechanochemistry: From Curiosity to Established Protocols. *Chem. Soc. Rev.* **2019**, *48*, 2274−2292.

(5) Gracin, D.; Štrukil, V.; Friščić, T.; Halasz, I.; Užarević, K. Laboratory Real-Time and In Situ Monitoring of Mechanochemical Milling Reactions by Raman Spectroscopy. *Angew. Chem.* **2014**, *126*, 6307−6311.

(6) Užarević, K.; Halasz, I.; Friščić, T. Real-Time and In Situ Monitoring of Mechanochemical Reactions: A New Playground for All Chemists. *J. Phys. Chem. Lett.* **2015**, *6*, 4129−4140.

(7) Batzdorf, L.; Fischer, F.; Wilke, M.; Wenzel, K.-J.; Emmerling, F. Direct In Situ Investigation of Milling Reactions Using Combined X-Ray Diffraction and Raman Spectroscopy. *Angew. Chem., Int. Ed.* **2015**, *54*, 1799−1802.

(8) Fischer, F.; Wenzel, K.-J.; Rademann, K.; Emmerling, F. Quantitative Determination of Activation Energies in Mechanochemical Reactions. *Phys. Chem. Chem. Phys.* **2016**, *18*, 23320−23325.

(9) Kulla, H.; Greiser, S.; Benemann, S.; Rademann, K.; Emmerling, F. In Situ Investigation of a Self-Accelerated Cocrystal Formation by Grinding Pyrazinamide with Oxalic Acid. *Molecules* **2016**, *21*, No. 917.

(10) Haferkamp, S.; Fischer, F.; Kraus, W.; Emmerling, F. Mechanochemical Knoevenagel Condensation Investigated in Situ. *Beilstein J. Org. Chem.* **2017**, *13*, 2010−2014.

(11) Lukin, S.; Stolar, T.; Tireli, M.; Blanco, M. V.; Babić, D.; Friščić, T.; Užarević, K.; Halasz, I. Tandem In Situ Monitoring for Quantitative Assessment of Mechanochemical Reactions Involving Structurally Unknown Phases. *Chem. - Eur. J.* **2017**, *23*, 13941−13949.

(12) Štrukil, V.; Gracin, D.; Magdysyuk, O. V.; Dinnebier, R. E.; Friščić, T. Trapping Reactive Intermediates by Mechanochemistry: Elusive Aryl N-Thiocarbamoylbenzotriazoles as Bench-Stable Reagents. *Angew. Chem., Int. Ed.* **2015**, *54*, 8440−8443.

(13) Lukin, S.; Tireli, M.; Lončarić, I.; Barišić, D.; Šket, P.; Vrsaljko, D.; di Michiel, M.; Plavec, J.; Užarević, K.; Halasz, I. Mechanochemical Carbon−Carbon Bond Formation That Proceeds via a Cocrystal Intermediate. *Chem. Commun.* **2018**, *54*, 13216−13219.

(14) Kulla, H.; Wilke, M.; Fischer, F.; Röllig, M.; Maierhofer, C.; Emmerling, F. Warming up for Mechanosynthesis − Temperature Development in Ball Mills during Synthesis. *Chem. Commun.* **2017**, *53*, 1664−1667.

(15) Kulla, H.; Haferkamp, S.; Akhmetova, I.; Röllig, M.; Maierhofer, C.; Rademann, K.; Emmerling, F. In Situ Investigations of Mechanochemical One-Pot Syntheses. *Angew. Chem., Int. Ed.* **2018**, *57*, 5930−5933.

(16) Carta, M.; Colacino, E.; Delogu, F.; Porcheddu, A. Kinetics of Mechanochemical Transformations. *Phys. Chem. Chem. Phys.* **2020**, *22*, 14489−14502.

(17) Sović, I.; Lukin, S.; Meštrović, E.; Halasz, I.; Porcheddu, A.; Delogu, F.; Ricci, P. C.; Caron, F.; Perilli, T.; Dogan, A.; Colacino, E. Mechanochemical Preparation of Active Pharmaceutical Ingredients Monitored by In Situ Raman Spectroscopy. *ACS Omega* **2020**, *5*, 28663−28672.

(18) Kuppler, R. J.; Timmons, D. J.; Fang, Q.-R.; Li, J.-R.; Makal, T. A.; Young, M. D.; Yuan, D.; Zhao, D.; Zhuang, W.; Zhou, H.-C. Potential Applications of Metal-Organic Frameworks. *Coord. Chem. Rev.* **2009**, *253*, 3042−3066.

(19) Sakamaki, Y.; Ozdemir, J.; Heidrick, Z.; Watson, O.; Shahsavari, H. R.; Fereidoonnezhad, M.; Khosropour, A. R.; Beyzavi, M. H. Metal−Organic Frameworks and Covalent Organic Frameworks as Platforms for Photodynamic Therapy. *Comments Inorg. Chem.* **2018**, *38*, 238−293.

(20) Ghanbari, T.; Abnisa, F.; Wan Daud, W. M. A. A Review on Production of Metal Organic Frameworks (MOF) for CO$_2$ Adsorption. *Sci. Total Environ.* **2020**, *707*, No. 135090.

(21) Stock, N.; Biswas, S. Synthesis of Metal-Organic Frameworks (MOFs): Routes to Various MOF Topologies, Morphologies, and Composites. *Chem. Rev.* **2012**, *112*, 933−969.

(22) Lee, Y.-R.; Kim, J.; Ahn, W.-S. Synthesis of Metal-Organic Frameworks: A Mini Review. *Korean J. Chem. Eng.* **2013**, *30*, 1667−1680.

(23) Zhao, N.; Cai, K.; He, H. The Synthesis of Metal−Organic Frameworks with Template Strategies. *Dalton Trans.* **2020**, *49*, 11467−11479.

(24) Stolar, T.; Užarević, K. Mechanochemistry: An Efficient and Versatile Toolbox for Synthesis, Transformation, and Functionaliza-

tion of Porous Metal−Organic Frameworks. *CrystEngComm* **2020**, *22*, 4511−4525.

(25) Lin, C.; Zhou, W.; Xiong, X.; Xuan, W.; Kitson, P. J.; Long, D.; Chen, W.; Song, Y.; Cronin, L. Digital Control of Multistep Hydrothermal Synthesis by Using 3D Printed Reactionware for the Synthesis of Metal−Organic Frameworks. *Angew. Chem.* **2018**, *130*, 16958−16962.

(26) Jones, C. L.; Hughes, C. E.; Yeung, H. H. M.; Paul, A.; Harris, K. D. M.; Easun, T. L. Exploiting in Situ NMR to Monitor the Formation of a Metal−Organic Framework. *Chem. Sci.* **2021**, *12*, 1486−1494.

(27) Karadeniz, B.; Žilić, D.; Huskić, I.; Germann, L. S.; Fidelli, A. M.; Muratović, S.; Lončarić, I.; Etter, M.; Dinnebier, R. E.; Barišić, D.; Cindro, N.; Islamoglu, T.; Farha, O. K.; Friščić, T.; Užarević, K. Controlling the Polymorphism and Topology Transformation in Porphyrinic Zirconium Metal−Organic Frameworks via Mechanochemistry. *J. Am. Chem. Soc.* **2019**, *141*, 19214−19220.

(28) Qin, Y.; Wen, P.; Voshage, M.; Chen, Y.; Schückler, P. G.; Jauer, L.; Xia, D.; Guo, H.; Zheng, Y.; Schleifenbaum, J. H. Additive Manufacturing of Biodegradable Zn-XWE43 Porous Scaffolds: Formation Quality, Microstructure and Mechanical Properties. *Mater. Des.* **2019**, *181*, No. 107937.

(29) Arabbaghi, E. K.; Mokhtari, J.; Naimi-Jamal, M. R.; Khosravi, A. Zn-MOF: An Efficient Drug Delivery Platform for the Encapsulation and Releasing of Imatinib Mesylate. *J. Porous Mater.* **2021**, *28*, 641−649.

(30) Karmakar, A.; Guedes da Silva, M. F. C.; Pombeiro, A. J. L. Zinc Metal−Organic Frameworks: Efficient Catalysts for the Diastereoselective Henry Reaction and Transesterification. *Dalton Trans.* **2014**, *43*, 7795−7810.

(31) Wang, L.; Zou, J.; Chen, S.; Yang, J.; Qing, F.; Gao, P.; Li, J. Zinc Terephthalates $ZnC_8H_4O_4$ as Anodes for Lithium Ion Batteries. *Electrochim. Acta* **2017**, *235*, 304−310.

(32) Qin, X.; Yang, W.; Yang, Y.; Gu, D.; Guo, D.; Pan, Q. A Zinc Metal−Organic Framework for Concurrent Adsorption and Detection of Uranium. *Inorg. Chem.* **2020**, *59*, 9857−9865.

(33) Friščić, T.; Reid, D. G.; Halasz, I.; Stein, R. S.; Dinnebier, R. E.; Duer, M. J. Ion- and Liquid-Assisted Grinding: Improved Mechanochemical Synthesis of Metal-Organic Frameworks Reveals Salt Inclusion and Anion Templating. *Angew. Chem., Int. Ed.* **2010**, *49*, 712−715.

(34) Getachew, N.; Chebude, Y.; Diaz, I.; Sanchez-Sanchez, M. Room Temperature Synthesis of Metal Organic Framework MOF-2. *J. Porous Mater.* **2014**, *21*, 769−773.

(35) Xing, J.; Schweighauser, L.; Okada, S.; Harano, K.; Nakamura, E. Atomistic Structures and Dynamics of Prenucleation Clusters in MOF-2 and MOF-5 Syntheses. *Nat. Commun.* **2019**, *10*, No. 3608.

(36) Schweighauser, L.; Harano, K.; Nakamura, E. Experimental Study on Interconversion between Cubic MOF-5 and Square MOF-2 Arrays. *Inorg. Chem. Commun.* **2017**, *84*, 1−4.

(37) Edgar, M.; Mitchell, R.; Slawin, A. M. Z.; Lightfoot, P.; Wright, P. A. Solid-State Transformations of Zinc 1,4-Benzenedicarboxylates Mediated by Hydrogen-Bond-Forming Molecules. *Chem. - Eur. J.* **2001**, *7*, 5168−5175.

(38) Hirai, Y.; Furukawa, K.; Sun, H.; Matsushima, Y.; Shito, K.; Masuhara, A.; Ono, R.; Shimbori, Y.; Shiroishi, H.; White, M. S.; Yoshida, T. Microwave-Assisted Hydrothermal Synthesis of ZnO and Zn-Terephthalate Hybrid Nanoparticles Employing Benzene Dicarboxylic Acids. *Microsyst. Technol.* **2018**, *24*, 699−708.

(39) Geranmayeh, S.; Abbasi, A.; Zarnani, A.-H.; Skripkin, M. Y. A Novel Trinuclear Zinc Metal−Organic Network: Synthesis, X-Ray Diffraction Structures, Spectroscopic and Biocompatibility Studies. *Polyhedron* **2013**, *61*, 6−14.

(40) Zhu, L.-N.; Zhang, L. Z.; Wang, W.-Z.; Liao, D.-Z.; Cheng, P.; Jiang, Z.-H.; Yan, S.-P. $[Zn(BDC)(H_2O)_2]_n$: A Novel Blue Luminescent Coordination Polymer Constructed from BDC-Bridged 1-D Chains via Interchain Hydrogen Bonds (BDC = 1,4-Benzenedicarboxylate). *Inorg. Chem. Commun.* **2002**, *5*, 1017−1021.

(41) Guilera, G.; Steed, J. W. Topological Control in Coordination Polymers by Non-Covalent Forces. *Chem. Commun.* **1999**, *2*, 1563−1564.

(42) Kaduk, J. A. *CCDC deposition number 1520407; Database identifier: ECATIO, Experimental Crystal Structure Determination*, 2016.

(43) Carton, A.; Mesbah, A.; Aranda, L.; Rabu, P.; François, M. New Metastable Hybrid Phase, $Zn_2(OH)_2(C_8H_4O_4)$, Exhibiting Unique Oxo-Penta-Coordinated Zn(II) Atoms. *Solid State Sci.* **2009**, *11*, 818−823.

(44) Carton, A.; Abdelouhab, S.; Renaudin, G.; Rabu, P.; François, M. Structure of Zinc Hydroxy-Terephthalate: $Zn_3(OH)_4(C_8H_4O_4)$. *Solid State Sci.* **2006**, *8*, 958−963.

(45) Rodríguez, N. A.; Parra, R.; Grela, M. A. Structural Characterization, Optical Properties and Photocatalytic Activity of MOF-5 and Its Hydrolysis Products: Implications on Their Excitation Mechanism. *RSC Adv.* **2015**, *5*, 73112−73118.

(46) Thirumurugan, A.; Rao, C. N. R. 1,2-, 1,3- and 1,4-Benzenedicarboxylates of Cd and Zn of Different Dimensionalities: Process of Formation of the Three-Dimensional Structure. *J. Mater. Chem.* **2005**, *15*, 3852.

(47) Zeleňák, V.; Vargová, Z.; Györyová, K. Correlation of Infrared Spectra of Zinc(II) Carboxylates with Their Structures. *Spectrochim. Acta, Part A* **2007**, *66*, 262−272.

(48) Hadjiivanov, K. I.; Panayotov, D. A.; Mihaylov, M. Y.; Ivanova, E. Z.; Chakarova, K. K.; Andonova, S. M.; Drenchev, N. L. Power of Infrared and Raman Spectroscopies to Characterize Metal-Organic Frameworks and Investigate Their Interaction with Guest Molecules. *Chem. Rev.* **2021**, *121*, 1286−1424.

(49) Habib, H. A.; Hoffmann, A.; Höppe, H. A.; Janiak, C. Crystal Structures and Solid-State CPMAS ^{13}C NMR Correlations in Luminescent Zinc(II) and Cadmium(II) Mixed-Ligand Coordination Polymers Constructed from 1,2-Bis(1,2,4-Triazol-4-Yl)Ethane and Benzenedicarboxylate. *Dalton Trans.* **2009**, *32*, 1742.

(50) Yuan, W.; Friščić, T.; Apperley, D.; James, S. L. High Reactivity of Metal-Organic Frameworks under Grinding Conditions: Parallels with Organic Molecular Materials. *Angew. Chem., Int. Ed.* **2010**, *49*, 3916−3919.

(51) Julien, P. A.; Užarević, K.; Katsenis, A. D.; Kimber, S. A. J.; Wang, T.; Farha, O. K.; Zhang, Y.; Casaban, J.; Germann, L. S.; Etter, M.; Dinnebier, R. E.; James, S. L.; Halasz, I.; Friščić, T. In Situ Monitoring and Mechanism of the Mechanochemical Formation of a Microporous MOF-74 Framework. *J. Am. Chem. Soc.* **2016**, *138*, 2929−2932.

(52) Lucier, B. E. G.; Chen, S.; Huang, Y. Characterization of Metal Organic Frameworks: Unlocking the Potential of Solid-State NMR. *Acc. Chem. Res.* **2018**, *51*, 319−330.

(53) Al-Terkawi, A.-A.; Scholz, G.; Prinz, C.; Emmerling, F.; Kemnitz, E. Ca-, Sr-, and Ba-Coordination Polymers Based on Anthranilic Acid via Mechanochemistry. *Dalton Trans.* **2019**, *48*, 6513−6521.

(54) O'Keefe, C. A.; Mottillo, C.; Vainauskas, J.; Fábián, L.; Friščić, T.; Schurko, R. W. NMR-Enhanced Crystallography Aids Open Metal−Organic Framework Discovery Using Solvent-Free Accelerated Aging. *Chem. Mater.* **2020**, *32*, 4273−4281.

(55) Hou, J.; Ashling, C. W.; Collins, S. M.; Krajnc, A.; Zhou, C.; Longley, L.; Johnstone, D. N.; Chater, P. A.; Li, S.; Coulet, M.-V.; Llewellyn, P. L.; Coudert, F.-X.; Keen, D. A.; Midgley, P. A.; Mali, G.; Chen, V.; Bennett, T. D. Metal-Organic Framework Crystal-Glass Composites. *Nat. Commun.* **2019**, *10*, No. 2580.

(56) Muratović, S.; Karadeniz, B.; Stolar, T.; Lukin, S.; Halasz, I.; Herak, M.; Mali, G.; Krupskaya, Y.; Kataev, V.; Žilić, D.; Užarević, K. Impact of Dehydration and Mechanical Amorphization on the Magnetic Properties of Ni(ii)-MOF-74. *J. Mater. Chem. C* **2020**, *8*, 7132−7142.

(57) Stolar, T.; Prašnikar, A.; Martinez, V.; Karadeniz, B.; Bjelić, A.; Mali, G.; Friščić, T.; Likozar, B.; Užarević, K. Scalable Mechanochemical Amorphization of Bimetallic Cu−Zn MOF-74 Catalyst for

Selective CO_2 Reduction Reaction to Methanol. *ACS Appl. Mater. Interfaces* **2021**, *13*, 3070−3077.

(58) Kong, X.; Terskikh, V. V.; Khade, R. L.; Yang, L.; Rorick, A.; Zhang, Y.; He, P.; Huang, Y.; Wu, G. Solid-State ^{17}O NMR Spectroscopy of Paramagnetic Coordination Compounds. *Angew. Chem., Int. Ed.* **2015**, *54*, 4753−4757.

(59) Bignami, G. P. M.; Davis, Z. H.; Dawson, D. M.; Morris, S. A.; Russell, S. E.; McKay, D.; Parke, R. E.; Iuga, D.; Morris, R. E.; Ashbrook, S. E. Cost-Effective ^{17}O Enrichment and NMR Spectroscopy of Mixed-Metal Terephthalate Metal−Organic Frameworks. *Chem. Sci.* **2018**, *9*, 850−859.

(60) Špačková, J.; Fabra, C.; Mittelette, S.; Gaillard, E.; Chen, C.-H.; Cazals, G.; Lebrun, A.; Sene, S.; Berthomieu, D.; Chen, K.; Gan, Z.; Gervais, C.; Métro, T.-X.; Laurencin, D. Unveiling the Structure and Reactivity of Fatty-Acid Based (Nano)Materials Thanks to Efficient and Scalable ^{17}O and ^{18}O-Isotopic Labeling Schemes. *J. Am. Chem. Soc.* **2020**, *142*, 21068−21081.

(61) Ashbrook, S. E.; Davis, Z. H.; Morris, R. E.; Rice, C. M. ^{17}O NMR Spectroscopy of Crystalline Microporous Materials. *Chem. Sci.* **2021**, *12*, 5016−5036.

(62) Martins, V.; Xu, J.; Wang, X.; Chen, K.; Hung, I.; Gan, Z.; Gervais, C.; Bonhomme, C.; Jiang, S.; Zheng, A.; Lucier, B. E. G.; Huang, Y. Higher Magnetic Fields, Finer MOF Structural Information: ^{17}O Solid-State NMR at 35.2 T. *J. Am. Chem. Soc.* **2020**, *142*, 14877−14889.

(63) Métro, T.; Gervais, C.; Martinez, A.; Bonhomme, C.; Laurencin, D. Unleashing the Potential of ^{17}O NMR Spectroscopy Using Mechanochemistry. *Angew. Chem., Int. Ed.* **2017**, *56*, 6803−6807.

(64) Chen, C.-H.; Gaillard, E.; Mentink-Vigier, F.; Chen, K.; Gan, Z.; Gaveau, P.; Rebière, B.; Berthelot, R.; Florian, P.; Bonhomme, C.; Smith, M. E.; Métro, T.-X.; Alonso, B.; Laurencin, D. Direct ^{17}O Isotopic Labeling of Oxides Using Mechanochemistry. *Inorg. Chem.* **2020**, *59*, 13050−13066.

(65) Chen, C.-H.; Goldberga, I.; Gaveau, P.; Mittelette, S.; Špačková, J.; Mullen, C.; Petit, I.; Métro, T.; Alonso, B.; Gervais, C.; Laurencin, D. Looking into the Dynamics of Molecular Crystals of Ibuprofen and Terephthalic Acid Using ^{17}O and ^2H Nuclear Magnetic Resonance Analyses. *Magn. Reson. Chem.* **2021**, *59*, 975−990.

(66) Schiffmann, J. G.; Emmerling, F.; Martins, I. C. B.; Van Wüllen, L. In-Situ Reaction Monitoring of a Mechanochemical Ball Mill Reaction with Solid State NMR. *Solid State Nucl. Magn. Reson.* **2020**, *109*, No. 101687.

(67) Kentgens, A. P. M.; Verhagen, R. Advantages of Double Frequency Sweeps in Static, MAS and MQMAS NMR of Spin I = 3/2 Nuclei. *Chem. Phys. Lett.* **1999**, *300*, 435−443.

(68) Iuga, D.; Schäfer, H.; Verhagen, R.; Kentgens, A. P. M. Population and Coherence Transfer Induced by Double Frequency Sweeps in Half-Integer Quadrupolar Spin Systems. *J. Magn. Reson.* **2000**, *147*, 192−209.

(69) Siegel, R.; Nakashima, T. T.; Wasylishen, R. E. Signal-to-Noise Enhancement of NMR Spectra of Solids Using Multiple-Pulse Spin-Echo Experiments. *Concepts Magn. Reson., Part A* **2005**, *26A*, 62−77.

(70) Brinkmann, A.; Kentgens, A. P. M. Proton-Selective $^{17}O−^1H$ Distance Measurements in Fast Magic-Angle-Spinning Solid-State NMR Spectroscopy for the Determination of Hydrogen Bond Lengths. *J. Am. Chem. Soc.* **2006**, *128*, 14758−14759.

(71) Massiot, D.; Fayon, F.; Capron, M.; King, I.; Le Calvé, S.; Alonso, B.; Durand, J.-O.; Bujoli, B.; Gan, Z.; Hoatson, G. Modelling One- and Two-Dimensional Solid-State NMR Spectra. *Magn. Reson. Chem.* **2002**, *40*, 70−76.

(72) Jameson, C. J. Reply to conventions for Tensor Quantities Used in Nuclear Magnetic Resonance, Nuclear Quadrupole Resonance and Electron Spin Resonance Spectroscopy. *Solid State Nucl. Magn. Reson.* **1998**, *11*, 265−268.

(73) Kresse, G.; Hafner, J. Ab Initio Molecular-Dynamics Simulation of the Liquid-Metal−Amorphous-Semiconductor Transition in Germanium. *Phys. Rev. B* **1994**, *49*, 14251−14269.

(74) Giannozzi, P.; Baroni, S.; Bonini, N.; Calandra, M.; Car, R.; Cavazzoni, C.; Ceresoli, D.; Chiarotti, G. L.; Cococcioni, M.; Dabo, I.; Dal Corso, A.; de Gironcoli, S.; Fabris, S.; Fratesi, G.; Gebauer, R.; Gerstmann, U.; Gougoussis, C.; Kokalj, A.; Lazzeri, M.; Martin-Samos, L.; Marzari, N.; Mauri, F.; Mazzarello, R.; Paolini, S.; Pasquarello, A.; Paulatto, L.; Sbraccia, C.; Scandolo, S.; Sclauzero, G.; Seitsonen, A. P.; Smogunov, A.; Umari, P.; Wentzcovitch, R. M. QUANTUM ESPRESSO: A Modular and Open-Source Software Project for Quantum Simulations of Materials. *J. Phys.: Condens. Matter* **2009**, *21*, No. 395502.

(75) Baroni, S.; de Gironcoli, S.; Dal Corso, A.; Giannozzi, P. Phonons and Related Crystal Properties from Density-Functional Perturbation Theory. *Rev. Mod. Phys.* **2001**, *73*, 515−562.

(76) Perdew, J. P.; Burke, K.; Ernzerhof, M. Generalized Gradient Approximation Made Simple. *Phys. Rev. Lett.* **1996**, *77*, 3865−3868.

(77) Troullier, N.; Martins, J. L. Efficient Pseudopotentials for Plane-Wave Calculations. *Phys. Rev. B* **1991**, *43*, 1993−2006.

(78) Kleinman, L.; Bylander, D. M. Efficacious Form for Model Pseudopotentials. *Phys. Rev. Lett.* **1982**, *48*, 1425−1428.

(79) Pickard, C. J.; Mauri, F. All-Electron Magnetic Response with Pseudopotentials: NMR Chemical Shifts. *Phys. Rev. B* **2001**, *63*, No. 245101.

(80) Lejaeghere, K.; Bihlmayer, G.; Björkman, T.; Blaha, P.; Blügel, S.; Blum, V.; Caliste, D.; Castelli, I. E.; Clark, S. J.; Dal Corso, A.; de Gironcoli, S.; Deutsch, T.; Dewhurst, J. K.; Di Marco, I.; Draxl, C.; Dułak, M.; Eriksson, O.; Flores-Livas, J. A.; Garrity, K. F.; Genovese, L.; Giannozzi, P.; Giantomassi, M.; Goedecker, S.; Gonze, X.; Grånäs, O.; Gross, E. K. U.; Gulans, A.; Gygi, F.; Hamann, D. R.; Hasnip, P. J.; Holzwarth, N. A. W.; Iuşan, D.; Jochym, D. B.; Jollet, F.; Jones, D.; Kresse, G.; Koepernik, K.; Küçükbenli, E.; Kvashnin, Y. O.; Locht, I. L. M.; Lubeck, S.; Marsman, M.; Marzari, N.; Nitzsche, U.; Nordström, L.; Ozaki, T.; Paulatto, L.; Pickard, C. J.; Poelmans, W.; Probert, M. I. J.; Refson, K.; Richter, M.; Rignanese, G.-M.; Saha, S.; Scheffler, M.; Schlipf, M.; Schwarz, K.; Sharma, S.; Tavazza, F.; Thunström, P.; Tkatchenko, A.; Torrent, M.; Vanderbilt, D.; van Setten, M. J.; Van Speybroeck, V.; Wills, J. M.; Yates, J. R.; Zhang, G.-X.; Cottenier, S. Reproducibility in Density Functional Theory Calculations of Solids. *Science* **2016**, *351*, 1415.

(81) Stievano, L.; Tielens, F.; Lopes, I.; Folliet, N.; Gervais, C.; Costa, D.; Lambert, J.-F. Density Functional Theory Modeling and Calculation of NMR Parameters: An Ab Initio Study of the Polymorphs of Bulk Glycine. *Cryst. Growth Des.* **2010**, *10*, 3657−3667.

(82) Colas, H.; Bonhomme-Coury, L.; Diogo, C. C.; Tielens, F.; Babonneau, F.; Gervais, C.; Bazin, D.; Laurencin, D.; Smith, M. E.; Hanna, J. V.; Daudon, M.; Bonhomme, C. Whewellite, $CaC_2O_4·H_2O$: Structural Study by a Combined NMR, Crystallography and Modelling Approach. *CrystEngComm* **2013**, *15*, 8840.

(83) Pyykkö, P. Year-2017 Nuclear Quadrupole Moments. *Mol. Phys.* **2018**, *116*, 1328−1338.

(84) Friščić, T.; Childs, S. L.; Rizvi, S. A. A.; Jones, W. The Role of Solvent in Mechanochemical and Sonochemical Cocrystal Formation: A Solubility-Based Approach for Predicting Cocrystallisation Outcome. *CrystEngComm* **2009**, *11*, 418−426.

(85) Bowmaker, G. A. Solvent-Assisted Mechanochemistry. *Chem. Commun.* **2013**, *49*, 334−348.

(86) Téllez S, C. A.; Hollauer, E.; Mondragon, M. A.; Castaño, V. M. Fourier Transform Infrared and Raman Spectra, Vibrational Assignment and Ab Initio Calculations of Terephthalic Acid and Related Compounds. *Spectrochim. Acta, Part A* **2001**, *57*, 993−1007.

(87) Varghese, H. T.; Panicker, C. Y.; Philip, D.; Sreevalsan, K.; Anithakumary, V. IR, Raman and SERS Spectra of Disodium Terephthalate. *Spectrochim. Acta, Part A* **2007**, *68*, 817−822.

(88) Embrechts, H.; Kriesten, M.; Ermer, M.; Peukert, W.; Hartmann, M.; Distaso, M. In Situ Raman and FTIR Spectroscopic Study on the Formation of the Isomers MIL-68(Al) and MIL-53(Al). *RSC Adv.* **2020**, *10*, 7336−7348.

(89) Stroh, J.; Ali, N. Z.; Maierhofer, C.; Emmerling, F. Ettringite via Mechanochemistry: A Green and Rapid Approach for Industrial Application. *ACS Omega* **2019**, *4*, 7734−7737.

(90) Harris, R. K.; Wasylishen, R. E.; Duer, M. J. *NMR Crystallography*; John Wiley & Sons, Ltd.: Chichester, UK, 2009.

(91) Bryce, D. L. NMR Crystallography: Structure and Properties of Materials from Solid-State Nuclear Magnetic Resonance Observables. *IUCrJ* **2017**, *4*, 350−359.

(92) Smith, M. E. Recent Progress in Solid-state Nuclear Magnetic Resonance of Half-integer Spin Low-γ Quadrupolar Nuclei Applied to Inorganic Materials. *Magn. Reson. Chem.* **2021**, *59*, 864−907.

(93) Leroy, C.; Szell, P. M. J.; Bryce, D. L. On the Importance of Accurate Nuclear Quadrupole Moments in NMR Crystallography. *Magn. Reson. Chem.* **2019**, *57*, 265−267.

(94) Leroy, C.; Bryce, D. L. Recent Advances in Solid-State Nuclear Magnetic Resonance Spectroscopy of Exotic Nuclei. *Prog. Nucl. Magn. Reson. Spectrosc.* **2018**, *109*, 160−199.

(95) Johnston, J. C.; Iuliucci, R. J.; Facelli, J. C.; Fitzgerald, G.; Mueller, K. T. Intermolecular Shielding Contributions Studied by Modeling the ^{13}C Chemical-Shift Tensors of Organic Single Crystals with Plane Waves. *J. Chem. Phys.* **2009**, *131*, No. 144503.

(96) No information regarding ″defect″ sites could be found in the X-ray diffraction data for the CCDC structure named ″ECATIO″.

(97) Pourpoint, F.; Gervais, C.; Bonhomme-Coury, L.; Azaïs, T.; Coelho, C.; Mauri, F.; Alonso, B.; Babonneau, F.; Bonhomme, C. Calcium Phosphates and Hydroxyapatite: Solid-State NMR Experiments and First-Principles Calculations. *Appl. Magn. Reson.* **2007**, *32*, 435−457.

(98) Reinholdt, M.; Croissant, J.; Di Carlo, L.; Granier, D.; Gaveau, P.; Bégu, S.; Devoisselle, J.-M.; Mutin, P. H.; Smith, M. E.; Bonhomme, C.; Gervais, C.; van der Lee, A.; Laurencin, D. Synthesis and Characterization of Crystalline Structures Based on Phenylboronate Ligands Bound to Alkaline Earth Cations. *Inorg. Chem.* **2011**, *50*, 7802−7810.

(99) Sene, S.; Reinholdt, M.; Renaudin, G.; Berthomieu, D.; Zicovich-Wilson, C. M.; Gervais, C.; Gaveau, P.; Bonhomme, C.; Filinchuk, Y.; Smith, M. E.; Nedelec, J.-M.; Bégu, S.; Mutin, P. H.; Laurencin, D. Boronate Ligands in Materials: Determining Their Local Environment by Using a Combination of IR/Solid-State NMR Spectroscopies and DFT Calculations. *Chem. - Eur. J.* **2013**, *19*, 880−891.

(100) Martins, V.; Xu, J.; Hung, I.; Gan, Z.; Gervais, C.; Bonhomme, C.; Huang, Y. ^{17}O Solid-state NMR at Ultrahigh Magnetic Field of 35.2 T: Resolution of Inequivalent Oxygen Sites in Different Phases of MOF MIL-53(Al). *Magn. Reson. Chem.* **2021**, *59*, 940−950.

(101) Bennett, T. D.; Todorova, T. K.; Baxter, E. F.; Reid, D. G.; Gervais, C.; Bueken, B.; Van de Voorde, B.; De Vos, D.; Keen, D. A.; Mellot-Draznieks, C. Connecting Defects and Amorphization in UiO-66 and MIL-140 Metal−Organic Frameworks: A Combined Experimental and Computational Study. *Phys. Chem. Chem. Phys.* **2016**, *18*, 2192−2201.

(102) Johansson, U.; Frost, R. L.; Forsling, W.; Kloprogge, J. T. Raman Spectroscopy of the Kaolinite Hydroxyls at 77 K. *Appl. Spectrosc.* **1998**, *52*, 1277−1282.

(103) Kolesov, B. Raman Investigation of H_2O Molecule and Hydroxyl Groups in the Channels of Hemimorphite. *Am. Mineral.* **2006**, *91*, 1355−1362.

(104) Yang, M.; Han, L.; Xu, Y.; Ke, H.; Zhou, N.; Dong, H.; Liu, S.; Qiao, G. Near Infrared Spectroscopic Study of Trioctahedral Chlorites and Its Remote Sensing Application. *Open Geosci.* **2019**, *11*, 815−828.

(105) Flakus, H. T.; Hachuła, B.; Hołaj-Krzak, J. T.; Al-Agel, F. A.; Rekik, N. "Long-Distance" H/D Isotopic Self-Organization Phenomena in Scope of the Infrared Spectra of Hydrogen-Bonded Terephthalic and Phthalic Acid Crystals. *Spectrochim. Acta, Part A* **2017**, *173*, 65−74.

(106) Lukin, S.; Tireli, M.; Stolar, T.; Barišić, D.; Blanco, M. V.; di Michiel, M.; Užarević, K.; Halasz, I. Isotope Labeling Reveals Fast Atomic and Molecular Exchange in Mechanochemical Milling Reactions. *J. Am. Chem. Soc.* **2019**, *141*, 1212−1216.